PAPER

Check for updates

Enhancing perovskite solar cell performance using a BaSnS₃ chalcogenide perovskite: a device simulation study

Mohammad Yasin Hayat Khan, [ID] [ab] Sayed Sahriar Hasan, [ID] *[c] Md. Zillur Rahman,[d] Md. Rasheduzzaman[ab] and Md. Zahid Hasan [ID] *[ab]

This study explores the potential of BaSnS₃, a tin-based chalcogenide perovskite, as a lead-free absorber material using density functional theory (DFT), where the hybrid functional HSE06 is utilized to investigate its structural, electronic, and optical properties. This compound exhibits dynamic stability with no imaginary phonon frequencies and possesses an indirect bandgap of 1.535 eV, making it well-suited for photovoltaic applications. Its favorable optical characteristics including a high absorption coefficient exceeding 10^5 cm^{-1} in the visible range and a static dielectric constant of 8.55 (unitless, relative to vacuum permittivity) further affirm its suitability as a solar absorber. In addition, comprehensive device simulations using SCAPS-1D are performed to evaluate the photovoltaic performance of BaSnS₃-based perovskite solar cells (PSCs) with various electron transport layers (ETLs) including ZnS, SnS₂, C₆₀, and LBSO. The ITO/ZnS/BaSnS₃/Pt structure demonstrates the highest efficiency, achieving a power conversion efficiency (PCE) of 25.93%, an open-circuit voltage (V_{OC}) of 1.136 V, and a short-circuit current density (J_{SC}) of 26.65 mA cm^{-2}. The influence of the absorber and ETL thickness, defect density, series and shunt resistances, and operating temperature on the cell performance is systematically analyzed. The findings reveal that the optimized absorber thickness (1.0 μm) and minimized defect density significantly enhance the efficiency. Furthermore, its temperature sensitivity and recombination dynamics are examined through quantum efficiency (QE), J–V analysis, and Mott–Schottky profiling. This combined theoretical and numerical investigation not only highlights BaSnS₃ as a promising candidate for future lead-free PSCs but also provides a foundation for further experimental validation and device engineering.

[a]*Materials Research and Simulation Lab, Department of Electrical and Electronic Engineering, International Islamic University Chittagong, Kumira, Chittagong, 4318, Bangladesh. E-mail: zahidhasan.02@gmail.com*

[b]*Department of Electrical and Electronic Engineering, International Islamic University Chittagong, Kumira, Chittagong, 4318, Bangladesh*

[c]*School of Information Science, JAIST, Nomi, Ishikawa, 923-1292, Japan. E-mail: sayedsahriarhasan@gmail.com*

[d]*Faculty of Electrical Engineering & Technology, Universiti Malaysia Perlis, Perlis, 02600, Malaysia*

1 Introduction

With the increase in world population and overall technological advancements, the energy demand is expected to reach 30 terawatts by the year 2050.[1] To compensate the high energy demand with minimum global effect, renewable energy sources have become a key study area. Solar energy is one of the most readily available energy sources, which can significantly contribute to the power demand, if harvested properly. In the search for improving reliable and sustainable solar energy harnessing sources, the key challenge is to achieve a high power conversion efficiency (PCE) with low production cost.[2] Si has been widely used as the main component in solar cell production. Unfortunately, conventional Si-based solar cells come with noticeable drawbacks such as the inability to convert specific wavelengths of light and the need for large amounts of raw materials and space to generate usable energy.[3] Constant studies for finding alternatives to traditional solar cells resulted in the discovery of perovskite solar cells (PSCs). These cells come with an exceptional absorption co-efficient and high carrier mobility and require less raw materials with simple manufacturing processes to produce high PCE.[4] As a result, sustainable energy sources have achieved a new dimension with the discovery of perovskite materials.[5] These promising attributes have motivated researchers to extend their studies on their PCE[6,7] as well as stability.[8,9] Since their initial development, the PCE of PSCs has improved remarkably from 3.8% in 2009 to 27.1% in 2025, according to the National Renewable Energy Laboratory (NREL).[10,11] This rapid progress has been driven by innovations in device architecture, interface engineering, and compositional tuning of the perovskite absorber layer. However, challenges related to long-term stability, lead toxicity, and scalability continue to motivate the search for

alternative materials. Perovskite compounds have the general structure ABX_3, where A is a monovalent cation, B is a divalent cation and X is an anion, which can be O, F, Cl, Br, I or S.[12–14,16] They generally crystallize in a cubic structure. Recent developments in perovskite solar cells (PSCs) have demonstrated significant performance improvements, driven by innovations in material composition, interface engineering, and tandem integration. For instance, single-junction inverted (p–i–n)-structured PSCs based on MA-Cs perovskite have demonstrated efficiencies up to 24.55% under the standard test conditions.[15] Moreover, according to the 2025 NREL efficiency chart, the certified PCEs have now reached 26.1% for single-junction PSCs, 34.9% for perovskite–Si tandem cells, and 30.1% for all-perovskite tandem cells.[11] These achievements reinforce the competitiveness of perovskite photovoltaics and underscore the growing need for environmentally stable and lead-free alternatives, such as chalcogenide perovskite materials. Their high-symmetry crystalline architectures and octahedral frameworks enhance exceptional photovoltaic transitions, while simultaneously exhibiting non-toxicity and environmental sustainability. The promise of tin-based perovskites is inherent in their structural adaptability and ability to achieve optimal band alignments. This adaptability promotes the refinement of the optical and electrical characteristics, thereby enhancing the charge transfer and light absorption. The combination of organic and inorganic perovskite materials, known as hybrid perovskites, shows impressive characteristics such as improved carrier lifetimes, better charge-carrier mobility and lower exciton binding energies.[17] However, their toxicity, instability and degradability limit their implementation in large-scale production.[18] Metal halide perovskite compounds have become the centre of attention due to their notable electronic and thermoelectric performance.[19] $CsXCl_3$ (X = Sn, Pb, and Ge) compounds have been proposed as lead-free alternatives due to their suitable narrow bandgaps, with calculated values of 1.5 eV, 2.4 eV, and 1.8 eV for X = Sn, Pb, and Ge using the GGA-PBE functional without spin–orbit coupling (SOC), and 0.7 eV, 1.7 eV, and 0.9 eV when SOC is included, respectively. These attributes prove their potential for PV applications.[20] Subsequently, $CsMF_3$ (M = Ge, Sn, and Pb) compounds have shown good thermoelectric performances for potential optoelectronic applications.[21] Sn-based perovskites have gained significant attention for their remarkable optoelectronic properties.[22–24] Additionally, they possess exceptional features such as tunable band gaps, dominant point defects, and small carrier effective masses.[25] Lead-based PSCs have a toxic effect on nature, which undermines their considerable efficiency.[26] As a result, research on alternatives to lead-based PSCs is in progress to minimize their adverse environmental effect. Noteworthy alternatives are halide perovskites,[27] halide double perovskites $(A_2B'B''X_6)$,[28] vacancy ordered perovskites (A_2BX_6)[29] and chalcogenide perovskites $(ABCh_3)$.[30] If the anion is O, S or Se, then the perovskite is known as chalcogenide perovskite. The general formula of chalcogenide perovskites shows the possibility of 3744 chalcogenide compounds with both cubic and orthorhombic structures, but only a limited number of compounds has the required thermodynamic

stability and capability to form in a certain order.[31] Studies show that Ge- and Sn-based PSCs can be suitable options due to their impressive nature such as low band gap, high carrier mobility and non-toxicity.[32] However, the high price and low availability of Ge[33] have motivated the study of Sn-based PSCs for photovoltaic (PV) applications. Chalcogenide PSCs have gained attention as a result of their impressive stability, non-toxicity and huge reservoir in nature.[34,35] These compounds possess higher absorption coefficients than other traditional perovskite compounds.[36] Many theoretical analyses have shown their potential PV applications as a result of their remarkable thermodynamic and atmospheric stability. One key feature of chalcogenide perovskites is that their wide band dispersions cause low effective mass, which ultimately aids in fast carrier mobility.[35] It is also seen that their absorption coefficient is greater than 10^5 cm^{-1},[36] which further strengthens their efficient PV performance. $BaSnS_3$ is a chalcogenide compound with the *Pnma* space group, which crystallizes in the orthorhombic phase. It forms a needle-like structure that is similar to NH_4-$CdCl_3$. $BaSnS_3$ is a suitable candidate for solar cell application due to a number of reasons. Firstly, it has a bandgap of 1.535 eV, which satisfies the ideal Shockley–Queisser (1.0–1.6 eV) range for an effective solar cell absorber.[37] Secondly, it exhibits impressive optical properties, including a high absorption coefficient exceeding 10^5 cm^{-1} in the visible region, and a static dielectric constant of ~8.55, all of which are favorable for efficient light absorption and charge separation in solar cells. Moreover, phonon dispersion calculations in previous theoretical studies confirm its dynamic stability, as indicated by the absence of imaginary phonon modes across the Brillouin zone. Furthermore, $BaSnS_3$ exhibits excellent charge transport characteristics, with electron mobility reported in the range of 20–40 cm^2 V^{-1} s^{-1} and hole mobility of around 10–25 cm^2 V^{-1} s^{-1}, making it a strong candidate for efficient carrier extraction in solar cell applications. Solar cell designs contain a standard planar configuration, where the absorber layer is place between the hole transport layer (HTL) and electron transport layer (ETL). The purpose of HTL is to properly transfer holes, while ETL facilitates the proper transmission of electrons. Additionally, transparent conducting oxides (TCOs) such as indium tin oxide (ITO) and fluorine-doped tin oxide (FTO) are commonly used as front electrodes in solar cells, offering high optical transparency and electrical conductivity to facilitate efficient photon entry and charge extraction. The absorber layer plays a vital role in achieving the optimum performance, and an additional layer is placed to support the absorber layer to achieve this. Furthermore, the desired performance is obtained by optimizing the layer, thickness, carrier concentrations and bulk defects. The charge mobility in the ETL plays a crucial role in enhancing the overall performance of the cell by elevating the fill factor (FF) and short-circuit current density (J_{SC}). Some common examples of ETLs are PCBM, C_{60}, SnS_2, TiO_2, ZnO, ZnS, LBSO and SnO_2.[38–41] Although TiO_2 has been shown to be a widely used ETL for achieving impressive solar cell performances,[42] it is associated with drawbacks such as instability when exposed to UV light.[43] Furthermore, a high temperature annealing process is required to produce this layer,[44] which

hinders its use as ETL in PSCs. As a result, the use of TiO_2 as ETL is avoided in this study. The quasi-one-dimensional-chalcogenide compound $BaSnS_3$ contains a suitable bandgap, which is ideal for solar cell application.[45,46] This serves as the motivation to study the optoelectronic performance as well as simulation of this material as an absorber to study its PV performance. Despite the growing interest in lead-free and thermally stable chalcogenide perovskites, the device-level simulation and performance analysis of $BaSnS_3$- based solar cells remain largely underexplored. Most previous works have focused on material-level DFT studies, with limited attention to how different transport layers and operating conditions influence the complete device behavior. Thus, to bridge this gap, the present work conducts a comprehensive numerical investigation using SCAPS-1D to evaluate the photovoltaic performance of $BaSnS_3$ as an absorber layer in combination with various ETL materials. In this work, an analytical approach using density functional theory (DFT) has been conducted to study the structural, electronic, optical and thermodynamic characteristics of the Sn-based chalcogenide compound $BaSnS_3$. Along with DFT, simulations on SCAPS-1D have also been conducted to analyze its photovoltaic performance. The PV characteristics of $BaSnS_3$ is analyzed by employing it as the absorber layer and ZnS, SnS_2, C_{60} and LBSO as the ETL layer. Its performance is evaluated by studying the necessary parameters such as layer thickness, interface defect density, bulk defect density, doping density, operating temperature, generation and recombination rates, current density–voltage (J–V), and quantum efficiency (QE). The comparative analysis highlights the optimum cell structure with highest efficiency. This study not only identifies promising transport layer configurations for efficient $BaSnS_3$-based solar cells but also provides insight into the device physics governing charge transport and recombination in these lead-free perovskite-inspired systems. Lastly, the performance of the studied structure is compared with other contemporary cell designs to estimate the future of solar cell technology. The findings contribute to the ongoing search for stable, non-toxic alternatives to lead halide perovskites and may guide future experimental efforts toward fabricating high-performance $BaSnS_3$ solar cells.

2 Materials and methodology

2.1 First principles calculations of $BaSnS_3$ absorber using DFT

First principles calculations were performed using the Vienna *Ab initio* Simulation Package (VASP)[47] to investigate the structural, electronic, and optical properties of $BaSnS_3$. Structural optimization was conducted using the Perdew–Burke–Ernzerhof (PBE) exchange-correlation functional, followed by electronic structure calculation using the HSE06 hybrid functional. The atomic core orbitals were examined through the projector augmented-wave (PAW) method.[48] The PAW potential core configurations were Ba: [Xe] $6s^2$, Sn: [Kr] $4d^{10}$, and S: [Ne] $3s^2$ $3p^4$. The cutoff energy was set to 400 eV. k-point sampling was carried out using the Monkhorst–Pack scheme with a k-mesh size of $13 \times 6 \times 3$. In the DOS calculations, denser k-meshes

were employed to ensure smoother graph results. The lattice vectors and atomic positions were stabilized until the interatomic forces were reduced to below 2.0×10^{-2} eV Å^{-1} and the energy convergence criteria were set to 1.0×10^{-6} eV. The dynamic stability of $BaSnS_3$ were evaluated through phonon vibrational computations using the density functional perturbation theory (DFPT) framework.[49] Several optical energy-dependent parameters such as absorption coefficient and reflectivity were analyzed for photon energies up to 50 eV, with the electric field polarization vectors aligned along the [100] direction.

2.2 SCAPS-1D numerical simulation

Device modelling and simulations were conducted using SCAPS-1D. The simulation is based on solving three core semiconductor equations, the continuity equations for holes and electrons and the position-dependent Poisson equation. These equations describe how charge carriers behave and interact within the solar cell.[50]

$$\frac{dP_n}{dt} = G_p - \frac{P_n - P_{n^0}}{\tau_p} - P_n u_p \frac{dE}{dx} - u_p E \frac{dP_n}{dx} + D_p \frac{d^2 P_n}{dx^2} \quad (1)$$

$$\frac{dn_P}{dt} = G_n - \frac{n_P - n_{p^0}}{\tau_n} - n_P u_n \frac{dE}{dx} - u_n E \frac{dn_P}{dx} + D_p \frac{d^2 n_P}{dx^2} \quad (2)$$

$$\frac{d}{dx}\left(\varepsilon(x)\frac{d\varnothing}{dx}\right) = q[p(x) - n(x) + N_{d^+}(x) - N_{a^-}(x) + p_t(x)$$
$$- n_t(x)] \quad (3)$$

The hole continuity equation (eqn (1)), the electron continuity equation (eqn (2)), and the Poisson equation (eqn (3)) are essential for understanding the transport of carriers and the electric field distribution throughout the device. In these equations, q represents the elementary charge of an electron, ε denotes the dielectric permittivity of the material, G is the carrier generation rate, D is the diffusion coefficient, Φ stands for the electrostatic potential, and E is the electric field. The symbols $p(x)$ and $n(x)$ refer to the concentrations of free holes and electrons at a given position x, while $p_t(x)$ and $n_t(x)$ represent the densities of trapped holes and electrons. N_d^+ and N_a^- correspond to the concentrations of ionized donor and acceptor dopants, respectively. The variable x indicates the position within the device structure, typically across its thickness. These parameters and equations form the mathematical foundation for accurately simulating the behavior of the solar cell under various conditions.

SCAPS-1D was employed to evaluate the performance of $BaSnS_3$-based solar cell architectures. The simulation began with the initialization of the software and definition of the cell structure, incorporating $BaSnS_3$ as the perovskite absorber and appropriate electron transport layers (ETLs). Essential material parameters such as bandgap, electron affinity, dielectric permittivity, and carrier mobilities were specified alongside the operational conditions including temperature, illumination under the AM 1.5 G spectrum, and a defined voltage bias range for analyzing current–voltage (J–V) characteristics. Key

performance metrics such as J–V characteristics, quantum efficiency (QE), capacitance, and Mott–Schottky behavior were selected for analysis. SCAPS-1D then solved the governing semiconductor equations, namely Poisson's equation, the continuity equations for electrons and holes, and drift-diffusion equations to simulate the electrical response of the device. The simulation results were analyzed using graphical tools such as OriginPro to interpret the output characteristics. The input material parameters used in this study were adopted from previously reported experimental data and are summarized in Tables 1 and 2. Table 1 outlines the fundamental physical and electronic properties of the layers used in the device, including indium-doped tin oxide (ITO), various ETLs, and the $BaSnS_3$ absorber. These parameters including bandgap, electron affinity, dielectric constant, and carrier mobility are critical for accurate SCAPS-1D simulations and strongly influence parameters such as open-circuit voltage (V_{OC}) and power conversion efficiency (PCE). In addition to the bulk layer properties, interfacial defects were also taken into account. Table 2 presents the interface-specific parameters such as defect density and carrier capture cross-sections. These interfacial characteristics are vital for understanding the recombination losses at the boundaries between different layers, which significantly affect the device efficiency. Optimization of the absorber layer was performed by evaluating various ETLs and contact combinations to identify the structure yielding the highest efficiency. All simulations were conducted at a standard operating temperature of 300 K (room temperature). The photovoltaic performance including open circuit voltage (V_{OC}), short-circuit current density (J_{SC}), fill factor (FF), and overall power conversion efficiency (PCE) was determined for each device design. Additionally, this study examined how modifications in absorber properties such as thickness, bandgap, electron affinity, and doping concentrations affect the operational performance of the solar cell.

2.3 BaSnS₃-based PSC structure

In this study, a planar heterojunction solar cell structure is simulated using SCAPS-1D. The device consists of a front contact, an electron transport layer (ETL), $BaSnS_3$ absorber, and a back contact. In this architecture, the ETL serves as the n-type layer, facilitating electron extraction and transport, while the $BaSnS_3$ layer exhibits p-type conductivity and acts as the primary light-absorbing and charge-generating layer. The full device configuration modeled is as follows:

$$Rb/ITO/ETL/BaSnS_3 \text{ (absorber)}/Pt$$

Here, Rb functions as the front electrode, Pt as the back contact, and four different materials are investigated as ETL candidates including ZnS, SnS_2, C_{60}, and La-doped $BaSnO_3$ (LBSO). The purpose of this study is to analyze how different ETL materials influence the overall device performance through energy alignment, defect interface behavior, and temperature-dependent characteristics. Upon exposure to light, excitons are formed, which are electron–hole pairs confined within the perovskite layer. These excitons can diffuse into both the n and p regions based on their diffusion lengths. At the interface between the n-type ETL and the p-type $BaSnS_3$ absorber, the excitons dissociate, with electrons moving toward the ETL and holes being transported through the absorber layer toward the back contact. The electric field between these layers aids in the dissociation of excitons and the movement of charge carriers. In the simulations, indium-doped tin oxide (ITO), $BaSnS_3$ perovskite, and platinum (Pt) were used as the transparent layer, perovskite layer, and back contact, respectively. To find the

Table 2 Interface parameters used in the simulation

Interface	ETL/BaSnS₃
Defect type	Neutral
Capture cross section for electrons (cm²)	1×10^{-19}
Capture cross section for holes (cm²)	1×10^{-19}
Energetic distribution	Single
Reference for defect energy level E_t	Above the highest EV
Energy concerning reference (eV)	0.600
Total density (cm³)	1×10^{10}

Table 1 Key parameters used in the SCAPS-1D simulation for each layer

Parameter	ITO[51]	ZnS[52]	SnS₂ (ref. 53)	C₆₀ (ref. 54)	LBSO[40]	BaSnS₃
Thickness (nm)	500	50	50	50	50	1000
Band gap, E_g (eV)	3.5	2.8	2.24	1.7	3.12	1.535
Electron affinity, χ (eV)	4.0	3.8	4.24	3.9	4.4	4.1
Dielectric permittivity (relative), ε_r	9.0	9.0	10	4.2	22	11.6094
CB effective density of states, N_c (cm⁻³)	2.2×10^{18}	2.2×10^{18}	2.2×10^{18}	8×10^{19}	1.8×10^{20}	1.675×10^{18}
VB effective density of states, N_v (cm⁻³)	1.8×10^{19}	1.8×10^{19}	1.8×10^{19}	8×10^{19}	1.8×10^{20}	8.594×10^{17}
Electron thermal velocity (cm s⁻¹)	1.00×10^7	1.00×10^7	1.00×10^7	1.00×10^7	1.00×10^7	1.00×10^7
Hole thermal velocity (cm s⁻¹)	1.00×10^7	1.00×10^7	1.00×10^7	1.00×10^7	1.00×10^7	1.00×10^7
Electron mobility, μ_n (cm²/Vs)	20	100	50	0.08	0.69	10.78
Hole mobility, μ_h (cm²/Vs)	10	25	50	0.035	0.69	16.81
Shallow uniform donor density, N_d (cm⁻³)	1×10^{21}	1×10^{19}	1×10^{16}	1×10^{17}	2×10^{21}	1×10^9
Shallow uniform acceptor density, N_a (cm⁻³)	0	1×10^6	0	0	0	1×10^{15}
Defect density, N_a (cm⁻³)	1×10^{15}	1×10^{15}	1×10^{15}	1×10^{15}	1×10^{15}	1×10^{15}
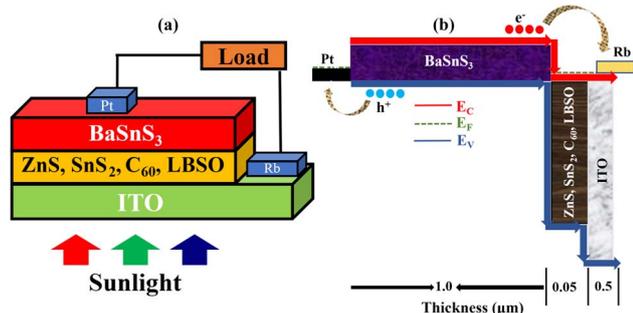
Fig. 1 (a) BaSnS$_3$-based device structure and (b) band alignment of ITO/ETLs/BaSnS$_3$.

Fig. 2 (a) Crystal structure of BaSnS$_3$. (b) Phonon dispersion curve of BaSnS$_3$.

perfect front and back metal contact of the solar cell, analysis of 8 front metal contacts and 8 back metal contacts was conducted, which yielded total of 64 combinations. Furthermore, 4 ETLs (Table 1) were investigated for the PSC to explore the best combination. Fig. 1(a) shows the solar device structure of the BaSnS$_3$ lead-free single perovskite absorber with 4 different combinations, highlighting its various layers. Fig. 1(b) depicts the band alignment of the solar cell design. The energy band alignment, including the electron and hole quasi-Fermi levels (F_n and F_p), respectively, along with the conduction band minimum (E_C) and valence band maximum (E_V), is illustrated. In all the configurations involving different ETLs, the hole quasi-Fermi level (F_p) closely aligns with the valence band edge (E_V), while the electron quasi-Fermi level (F_n) remains consistent with the conduction band edge (E_C). Among the heterojunction architectures studied, all ETLs except for C$_{60}$ exhibit nearly identical device performances. This is primarily attributed to the similarity in their energy bandgaps, which leads to comparable electronic behavior in the device structures. The simulations were conducted at a frequency of 1 MHz and a working temperature of 300 K, under the AM 1.5 G solar spectrum with an incident power density of 1000 mW cm^{-2}.

3 Result and discussion

3.1 DFT result analysis

3.1.1 Structural properties and dynamic stability of BaSnS$_3$.
The structural properties of a material are crucial for understanding its basic crystal structure as well as the placements of various atoms to create bonds. It also provides the volume of the crystal structure. BaSnS$_3$ belongs to the *Pnma* (62) space group in an orthorhombic crystal structure.[55] Its structure is similar to that of PbZrS$_3$,[56] and MSnS$_3$ (M = Zr and Hf).[57] Fig. 2(a) shows the optimized conventional crystal structures of BaSnS$_3$. To obtain the structural properties of BaSnS$_3$, the GGA-PBE method is applied due to its impressive accuracy. The atomic positions of Ba (4c), Sn (4c), and S (4c) were implemented for structure generation and optimization. 4c of Ba is (0.076, 0.75, 0.826), whereas 4c of Sn for this material is (0.167, 0.25, 0.556). 4c of S1, S2, S3 is (0.027, 0.25, 0.400), (0.163, 0.25, 0.997) and (0.212, 0.75, 0.207), respectively. The values of the *a, b, c* lattice constants for BaSnS$_3$ are 3.98874 Å, 8.63226 Å and
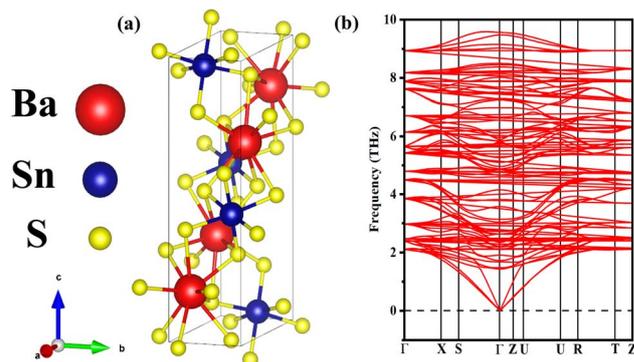
14.78784 Å, respectively, and the volume of the compound is around 509.1727 Å^3.

The phonon dispersion curve is crucial to understand the thermodynamic stability of a compound and helps to predict its application in the field of time-dependent external influences. Fig. 2(b) depicts the precise phonon band structures of BaSnS$_3$, which analyze its structural stability. The horizontal axis of the plot indicates the high symmetry points of the Brillouin zone, while the vertical axis indicates the phonon frequency in THz. The high symmetry points in the Brillouin zone for our calculation are (Γ-X-S-Γ-Z-U-U-R-T-Z). Phonons are quanta of vibrational energy, which represent the collective atomic vibrations inside the lattice. Phonons affect numerous processes such as heat transmission, electrical conductivity and thermal growth of materials. The vibrational modes are sectioned in different parts. Some of these modes are known as acoustic mode and converge gamma points in the low frequency region. The remaining modes are known as optic modes and operate in the high frequency region. According to Fig. 2(b), it is clear that the dispersion shows a positive frequency for all the compounds throughout the Brillouin zone, which indicates their dynamic stability.[58,59] The modes for all the compounds are spread across several branches with the highest frequency reaching up to 10 THz. It is noteworthy to mention that the imaginary frequency in the phonon dispersion curve indicates the structural instability of a compound.[60]

3.1.2 Band structure and density of states of BaSnS$_3$.
Electronic properties include the electronic band structure (BS) and density of states (DOS), which are related to the charge density and provide insights into whether a material is metal, insulator or semiconductor.[61,62] These classifications are performed based on the electron path flow changes that occur at the Fermi level (E_F). The BS is comprised of electronic, optical and opto-electronic behaviors, and often requires tuning with regards to the desired purpose.[63] Fig. 3(a) depicts the electronic band structure of BaSnS$_3$. The band structures of the orthorhombic-structured BaSnS$_3$ are along the initial Brillouin zones between −5 eV to 5 eV energy, along with their high symmetry directions (Γ-X-S-Γ-Z-U-R-T), respectively. These symmetry points are along the horizontal axis and reflect the wave vector (K) in different high symmetry points of the bulk
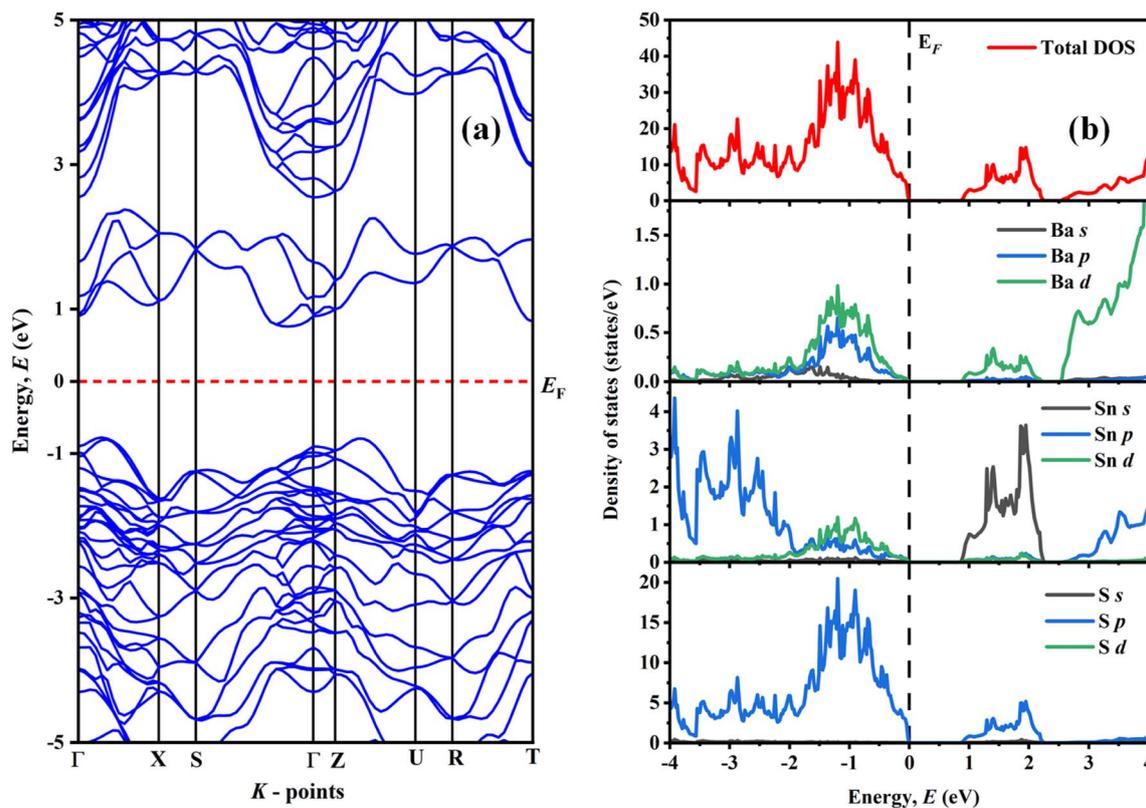
Fig. 3 (a) Electronic band structure and (b) total and partial DOS of BaSnS₃.

Brillouin zone. The vertical axis represents the energy levels, where the 0 eV red dotted line represents the Fermi level (E_F). E_F divides the energy spectrum into two sections, where the upper section is called the conduction band and the lower section is called the valence band.

The band gap is the difference between the conduction band minimum (CBM) and valence band maximum (VBM). It helps to estimate the efficiency of a material when implemented in solar cells. The Shockley–Queisser (S.Q.) limit indicates that 1.4 eV is the optimum bandgap for achieving the maximum theoretical efficiency for a single-junction solar cell and is related to the maximum light conversion efficiency.[64] The calculated bandgap of BaSnS₃ is 1.535 eV, which indicates its semiconducting nature as well as it is a good candidate for solar cell and other opto-electronic applications due to its narrow bandgap. The positions of the valence band maximum (VBM) and conduction band minimum (CBM) at different symmetry points indicate that this compound is an indirect bandgap semiconductor. Indirect bandgap semiconductors possess properties such as weaker light absorption, less heat generation and durability. These properties are used in thin film solar cells.[65–67]

Fig. 3(b) depicts the calculated total density of states (TDOS) and partial density of states (PDOS) with atomic contributions for different orbitals around E_F. They are crucial for providing adequate observation regarding the electron configuration as well as atomic bonding of a material. The whole material contributes to the formation of both the valence (VB) and

conduction band (CB), while the majority of its contribution is to the valence band. No peak at E_F solidifies the idea that this material is semiconductor. The Ba-d orbital contributions form the conduction band with ~4 eV (~2 states per eV). The major contribution of Sn-p at ~ −4 eV (~4 states per eV) to form VB and Sn-s at ~2 eV (~4 states per eV) to form CB can be seen. The major contribution of S-p to form VB for BaSnS₃ is observed and a slight contribution for CB can also be seen.

3.1.3 Optical properties of BaSnS₃. The optical properties of a compound are crucial for understanding its potential in the field of photonics as well as optoelectronics. This is done by analyzing its response when electromagnetic waves of various energy levels are incident on it. Several key optical properties such as absorption co-efficient, reflectivity, refractivity and loss function are analyzed for BaSnS₃ along the [100] direction and photon energy range up to 14 eV. Fig. 4(a and b) depict the output optical characteristics of this compound under the above-mentioned conditions.

The absorption coefficient characterizes the electromagnetic energy absorption of a compound.[68] It further gives an assumption of the solar energy conversion rate of the compound. The absorption coefficient, denoted by $\alpha(\omega)$, is obtained from the real and imaginary part of the dielectric function, as follows:[69]

$$\alpha(\omega) = \sqrt{2}\omega \left[\sqrt{\varepsilon_1^2(\omega) + \varepsilon_2^2(\omega)} - \varepsilon_1(\omega) \right]^{\frac{1}{2}} \quad (4)$$
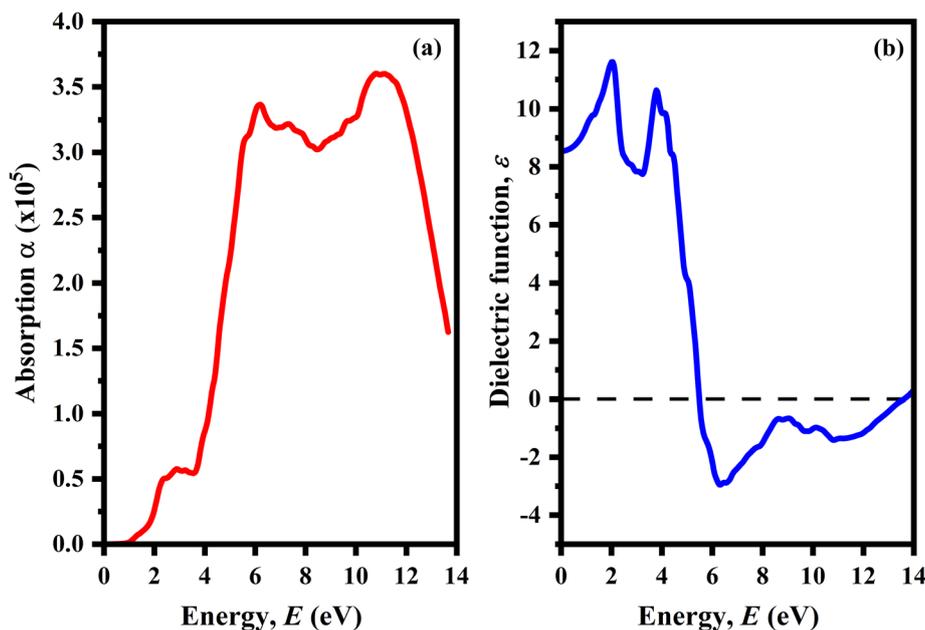
Fig. 4 (a) Absorption coefficient and (b) dielectric function of BaSnS$_3$.

Fig. 4(a) shows the absorption coefficient of BaSnS$_3$. In the lower range of 0 to 1 eV, almost no absorption is found. In the range of 2 to 6 eV, the absorption rate of all the materials keeps increasing and peaks are found in the range of 10 to 12 eV energy. The highest peak is found for BaSnS$_3$ at around 11 eV. The peaks in the visible range suggest the possible application of BaSnS$_3$ in the solar and photonic industry.

This study focuses on the optical properties of BaSnS$_3$ in the interband region. The analysis primarily considers the interband optical transitions, given that they dominate the dielectric response in this spectral range. Indirect intraband transitions were excluded from the investigation due to their reliance on phonon participation, which involves a relatively low scattering cross-section compared to direct transitions. As a result, phonon-assisted momentum conservation was deemed unnecessary. The dielectric function of a material describes its response to incident electromagnetic radiation. At zero photon energy, this response is represented by the static dielectric function, a critical parameter for assessing the performance of optoelectronic devices. A higher static dielectric constant typically correlates with lower charge carrier recombination rates, thereby contributing to improved device efficiency.[70,71] The static dielectric constant, $\varepsilon(0)$, characterizes the response of a material to an external electromagnetic field at zero photon energy. This parameter is significant in determining the charge carrier recombination rates and the efficiency of optoelectronic devices. Notably, an inverse relationship between $\varepsilon(0)$ and the optical bandgap is frequently observed, whereby materials with smaller bandgaps tend to exhibit higher static dielectric constants.

The dielectric function, $\varepsilon(\omega)$, is a complex function representing the optical behavior of a material and is composed of two parts, the real part, $\varepsilon_1(\omega)$, associated with polarization in response to an external field, and the imaginary part, $\varepsilon_2(\omega)$,

which describes the light absorption characteristics of a material. This relationship is expressed as follows:

$$\varepsilon(\omega) = \varepsilon_1(\omega) + i\varepsilon_2(\omega) \tag{5}$$

The real part, $\varepsilon_1(\omega)$, is typically determined using the Kramers–Kronig transformation, as follows:[72]

$$\varepsilon_1(\omega) = 1 + \frac{2}{\pi} p \int_0^\infty \frac{\alpha_{\omega' *\varepsilon_2}(\omega')}{\omega'^2 - \omega^2} \, d\omega \tag{6}$$

The imaginary part, $\varepsilon_2(\omega)$, is calculated using a quantum mechanical formalism derived from the Kohn–Sham approach, as follows:[73]

$$\varepsilon_2(\omega) = \frac{2\pi e^2}{\Omega\varepsilon_0} \sum_{k,v,c} \left|\Psi_k^c|\hat{u} \times \vec{r}|\Psi_k^v\right|^2 \delta\left(E_k^c - E_k^v - E\right) \tag{7}$$

In eqn (6), p denotes the principal value of the integral. In eqn (7), the symbols are Ω (unit cell volume), e (elementary charge), ε_0 (vacuum permittivity), Ψ_k^V and Ψ_k^c (valence and conduction band wave functions), and r (position operator). The dielectric response of BaSnS$_3$, as depicted in Fig. 4(b), shows that the real part, $\varepsilon_1(\omega)$, increases sharply in the visible energy range, reaching a maximum value of 11.6 at 3.55 eV, followed by a decline up to approximately 6 eV, and then a gradual increase. The static dielectric constant was calculated to be 8.55, a value within the typical range (2–10) observed in promising optoelectronic materials.[74] A higher $\varepsilon_1(0)$ generally correlates with a reduction in charge carrier recombination, enhancing the device performance. At photon energies near 5.5 eV, the material exhibits negative values of $\varepsilon_1(\omega)$, indicating the onset of metallic behavior. At these energy levels, BaSnS$_3$ reflects incident photons, making it suitable for potential use in reflective coatings or optical filters.

3.2 Simulated results for BaSnS₃-based solar cell

3.2.1 Effect of front and back contact on solar cell efficiency. The contacts of a solar cells play a crucial role in effectively transporting carriers to harness energy.[75] To select a material to be used as a contact for optimum performance, the contacts should have low resistance for ensuring high electricity generation. Furthermore, the contacts should be selected considering that they do not react with absorber or other layers and remain stable for longevity. A bad contact can induce various issues such as low energy extraction, less active area, and shading, while an optimized contact can improve the above-mentioned conditions along with reduced recombination, which ultimately updates the overall performance of the SC. Fig. 5(a–d) depict the effect of various metal layers used as the front and back contact in the overall performance of the analyzed cell design. The analysis consisted of 8 front and 8 back contacts, which give a total of 64 combinations of gadgets. The work function (W_F) of the contacts plays the main role in the overall output of the cell. It is confirmed from the analysis that Pt and Rb is ideal as the left and right contacts, respectively, for the simulated cell design due to their impressive overall performance across all the output parameters. This combination yields the maximum PCE of 25.94%, V_{OC} of 1.14 V, J_{SC} of 26.66 mA cm^{-2} and FF of 85.58%.

3.2.2 Energy band diagram. Fig. 6(a–d) illustrate the energy diagram of the four optimized PSCs based on BaSnS₃. To separate the electrons at the ETL and BaSnS₃ interface, the ETL electron affinity must be larger than BaSnS₃. The energy band variation at these interfaces significantly impacts the device performance parameters (Fig. 6). In Fig. 6(a–d), the quasi-Fermi levels of each device coexist with the conduction band energy (E_C) and valence band energy (E_V). The F_p of each ETL coincides with the E_V, while F_n and E_C exhibit harmonious alignment. BaSnS₃ has a band gap of 1.535 eV, while the band gaps of the ZnS, SnS₂, C₆₀, and LBSO ETLs are 2.8, 2.24, 1.7, and 3.12 eV, respectively. Due to their similar band alignment, the performance of ZnS, and C₆₀ ETLs is comparable. Similar characteristics can be seen for SnS₂ and LBSO. Fig. 6(a) and (d) exhibit their high potential and their band gaps, making them suitable for capturing a significant portion of the solar spectrum, respectively. When considering different thicknesses from 0.1 μm to 1.2 μm, there is a trade-off, where a thicker layer can enhance light absorption but may lead to increased series resistance. Fig. 6(c) may face challenges in terms of light absorption due to the small band gap (1.7 eV) and potentially limited thickness (0.05 μm) of its ETL. Although Fig. 6(a) has a band gap that is close to that in Fig. 6(b), further investigation is required to determine the optimal balance between light absorption and resistance. Overall, Fig. 6(a) demonstrates potential and warrants further exploration. These analyses enable the adjustment of thickness to improve the light absorption as well as potentially minimize the resistance, which results in higher efficiency in converting solar energy.
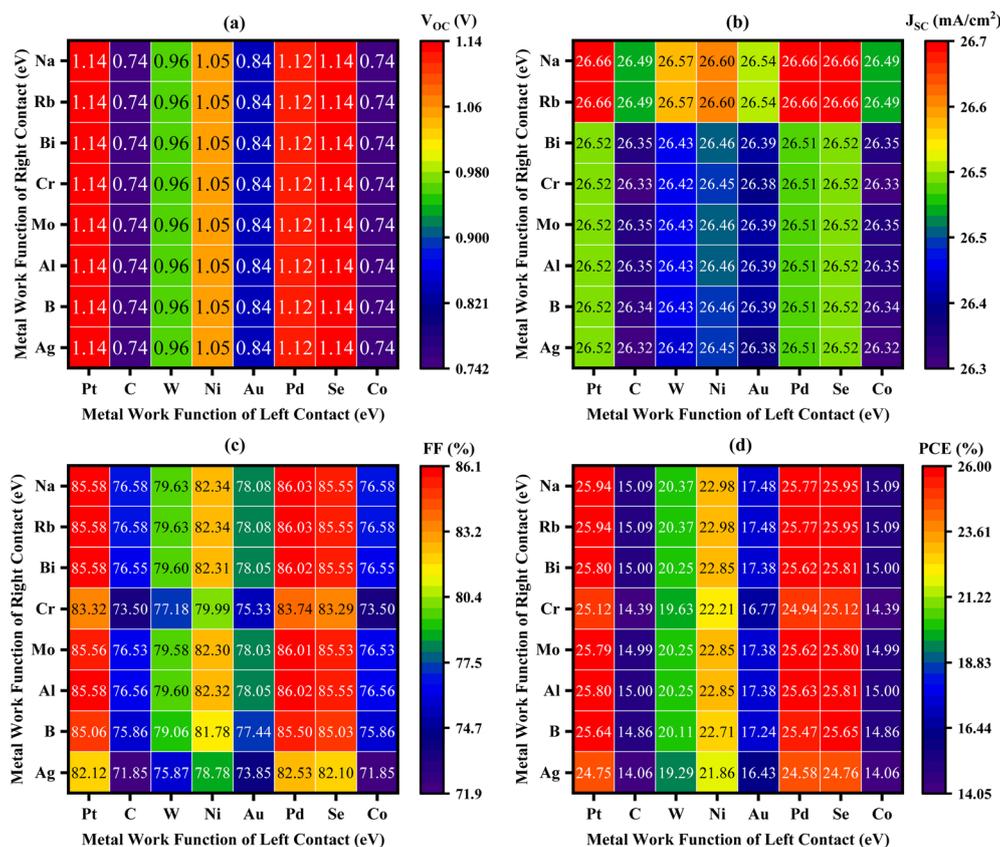

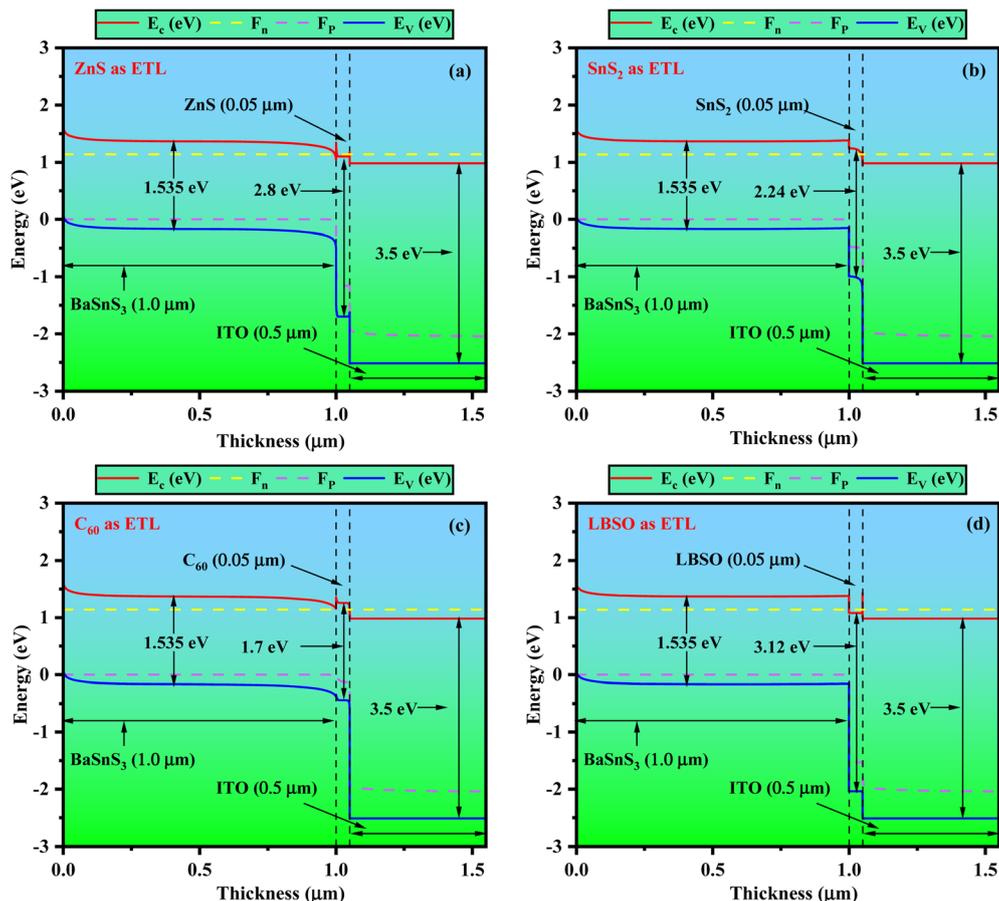**Fig. 5** Effect of contact on the device (a) V_{OC}, (b) J_{SC}, (c) FF, and (d) PCE.

© 2025 The Author(s). Published by the Royal Society of Chemistry

Fig. 6 Energy band diagrams of solar cell designs with (a) ZnS, (b) SnS$_2$, (c) C$_{60}$, and (d) LBSO ETLs.

3.2.3 Influence of changing absorber and ETL thickness. This analysis explains the crucial role of the absorber layer and ETL thickness in improving the performance of solar cells. This optimization is not merely a technical detail but a pivotal factor in attaining the optimal performance in SCs. In our investigation, the absorber and ETL thickness were varied from 0.4 to 1.2 µm and 0.03 to 0.1 µm, respectively, to assess their impact on the PV performance of the four optimized perovskite solar cells (Fig. 7–10). Fig. 7(a–d) illustrate how the variation in the BaSnS$_3$ absorber and ETL thickness influences the open-circuit voltage (V_{OC}) of the cell structures under examination, as depicted by the contour plots. It is intriguing to note that all the cell structures contain an identical pattern in their ETL. This pattern remained consistent even when the thickness of the absorber and ETL was altered. The V_{OC} values reached their peak when the absorber thickness was between 0.4 µm to 0.5 µm, and the ETL thickness was between 0.04 µm 0.06 µm for all the structures. In contrast, the ITO/SnS$_2$/BaSnS$_3$/Pt-based SCs exhibited the highest V_{OC} value when the absorber thickness was approximately 0.4 µm and the ETL thickness was around 0.06 to 0.1 µm (Fig. 7(b)). In all the structures, the variation in ETL thickness was not a significant factor. Elevation of the absorber thickness resulted in a decline in the V_{OC} of these three structures. All the structures showed pretty close V_{OC} with ITO/C$_{60}$/BaSnS$_3$/Pt having the lowest value of 1.177 V (Fig. 7(c)).

Fig. 8(a–d) illustrate how variation in the BaSnS$_3$ and ETL layer thicknesses affect J_{SC} for the analyzed solar cell configurations. The maximum J_{SC} value (26.94 mA cm^{-2}) is obtained when ZnS, SnS$_2$, and LBSO were employed as ETL and the absorber thickness was in the range of 1.0–1.2 µm (Fig. 8(a), (b) and (d)). In these configurations, the ETL thickness does not affect their performance. In the case of the C$_{60}$-based structure, a certain range of absorber thickness (0.7 µm to 1.2 µm) and ETL thickness (0.03 µm to 0.05 µm) will generate the maximum output (Fig. 8(c)). Among them, the J_{SC} value for the ITO/C$_{60}$/BaSnS$_3$/Pt structure was the lowest (26.50 mA cm^{-2}) (Fig. 8(c)). The J_{SC} values for each SC increased with the absorber layer thickness due to the increase in spectral sensitivity at longer wavelengths. The short-circuit current density (J_{SC}) is fundamentally determined by the number of photons absorbed by the absorber and the efficiency at which the photogenerated electron–hole pairs are collected.[76] In these device structures, the BaSnS$_3$ layer serves as the primary absorber layer for incident sunlight, as evidenced by its high absorption coefficient (Fig. 4(a)). The spectral absorption profile of the BaSnS$_3$ absorber dictates the initial generation of electron–hole pairs. As shown in Fig. 4(a), BaSnS$_3$ exhibits strong absorption in the visible range, with the absorption rates rising significantly between 2 to 6 eV. The QE curve shown in Fig. 17(b) provides a direct quantitative link to this absorption and subsequent
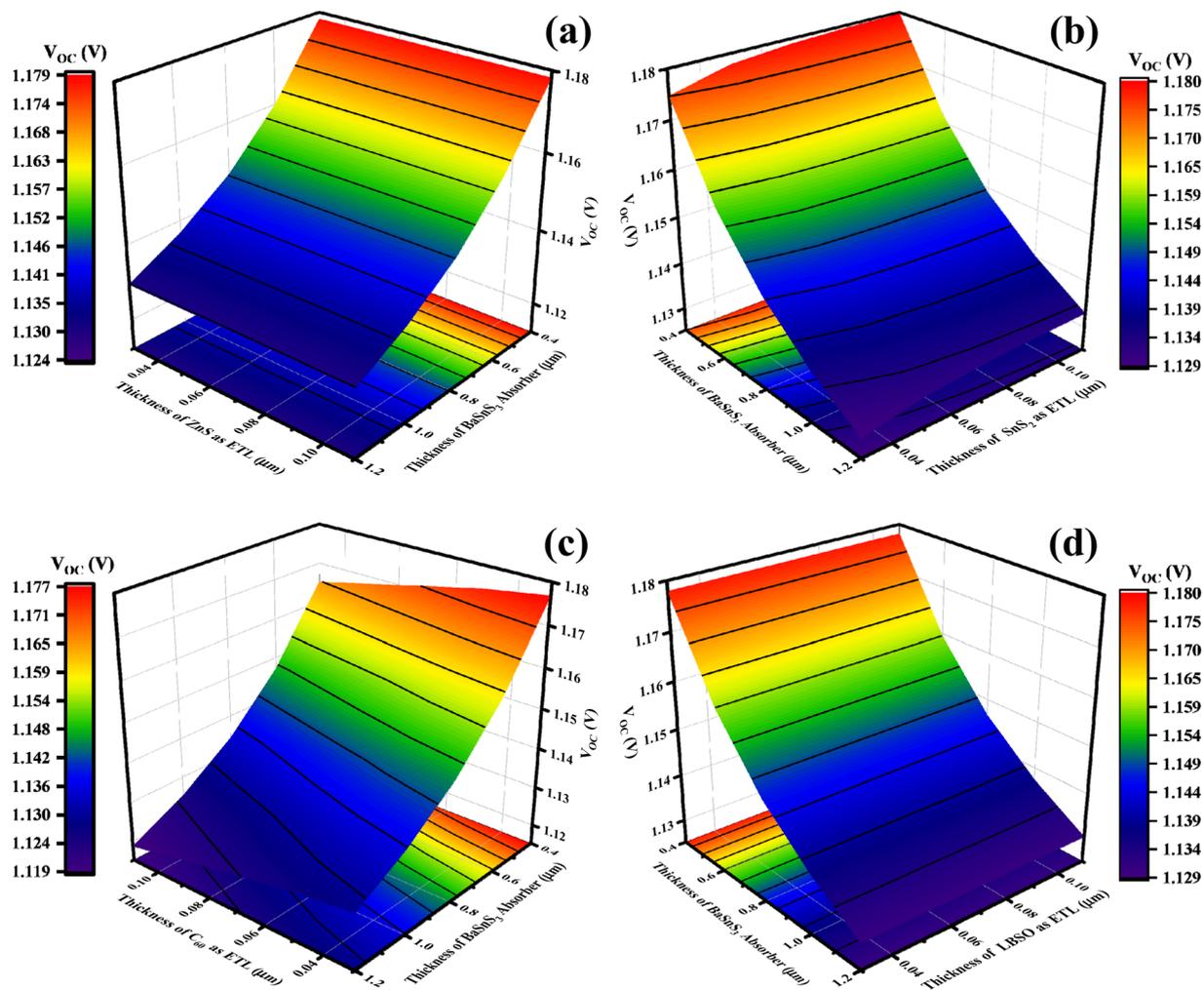
Fig. 7 Contour mapping of V_{OC} (V) with (a) ZnS, (b) SnS$_2$, (c) C$_{60}$, and (d) LBSO ETLs.

carrier collection. In the ZnS-, SnS$_2$-, and LBSO-based designs, the QE values start at around 98%, peak near 100%, and then gradually decline to zero at around 800 nm. This near-unity QE over a broad spectral range (from roughly 350 nm to 750 nm) indicates highly efficient photon absorption by the BaSnS$_3$ absorber and nearly perfect collection of the generated carriers within this region. Given that the ETLs are thin and primarily function to transport electrons to the ITO electrode and block holes, their own absorption contributions are negligible compared to the thick BaSnS$_3$ absorber. The consistent J_{SC} values across the ZnS, SnS$_2$, and LBSO ETLs confirm that these ETLs effectively extract the electrons generated in the BaSnS$_3$ absorber layer. Their conduction band minima (CBM) are well-aligned with the CBM of BaSnS$_3$, creating a favorable energy step for electron transfer, while blocking holes, as seen in Fig. 1(b) and 6(a, b, and d). This ensures that the majority of photogenerated carriers from the absorber are collected efficiently, regardless of which of these three ETLs is used. The slight deviation for C$_{60}$ further supports this interpretation. Although C$_{60}$ also functions as an ETL, its initial QE value is lower (50%) and peaks at around 92% at 720 nm, which can be

seen in Fig. 17(b). This lower QE in certain spectral regions implies the slightly less efficient collection of photogenerated carriers, either due to less favorable band alignment (Fig. 6(c)) or potentially lower carrier mobility compared to the other inorganic ETLs, as seen in Table 1. Consequently, it yields a marginally lower J_{SC}. Therefore, the consistent J_{SC} across the ZnS, SnS$_2$, and LBSO ETLs signifies that the overall photogeneration and collection efficiency are predominantly dictated by the optical properties and thickness of the absorber, rather than the substantial differences in ETL absorption or their electron transport properties once the carriers reach the ETL/absorber interface. The high and broad QE of the devices confirms that the BaSnS$_3$ absorber efficiently harvests most of the usable photons, leading to a consistent maximum current output.

Fig. 9(a–d) illustrate the impact of the BaSnS$_3$ and ETL layer thickness on the FF values for various SC designs. Upon examination of the contour plots of the four different solar device architectures, it is evident that the ITO/ZnS/BaSnS$_3$/Pt-based electron transport layer (ETL) structures exhibit a wide range of high-efficiency zones (Fig. 9(a)). The peak range of fill
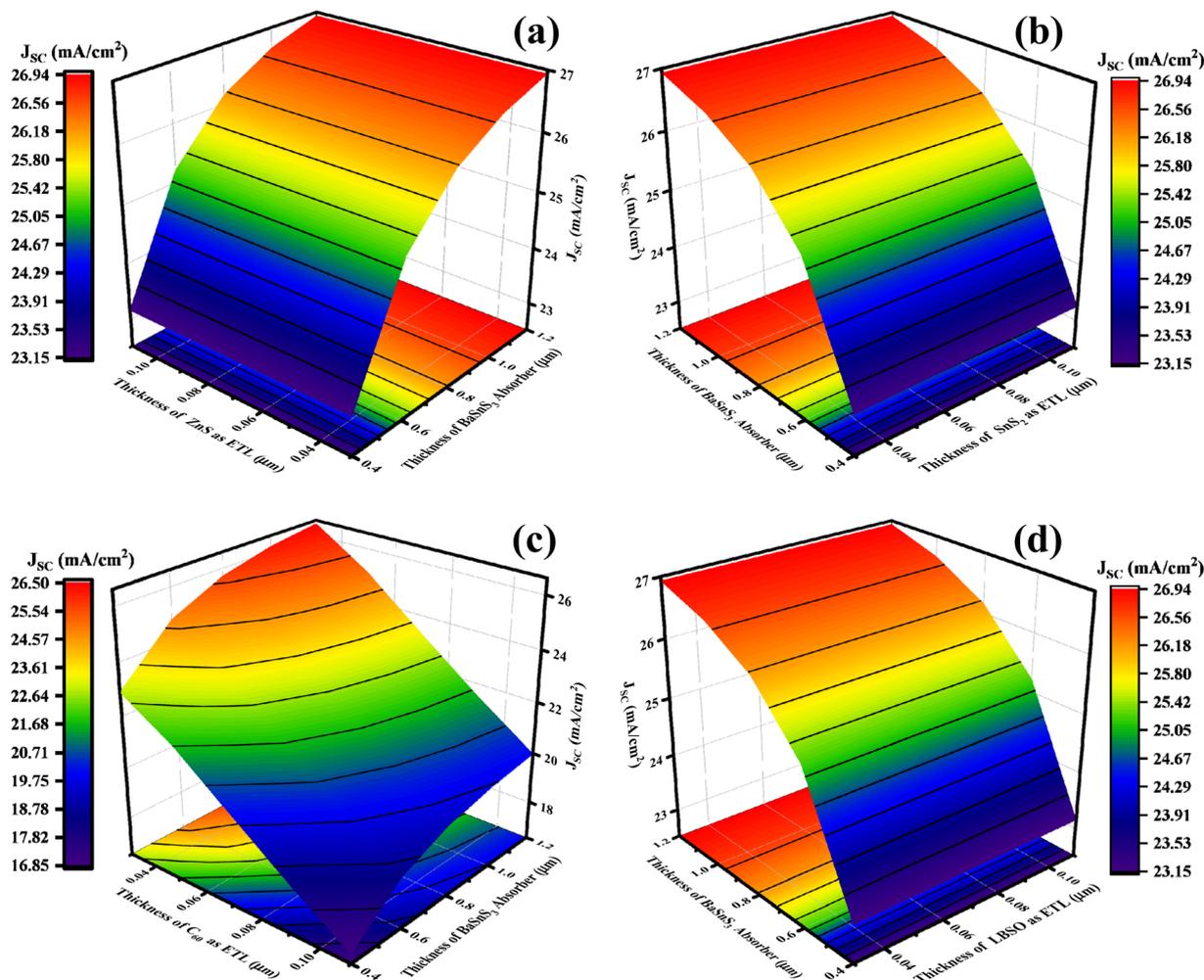
Fig. 8 Contour plots of J_{SC} (mA cm^{-2}) with (a) ZnS, (b) SnS$_2$, (c) C$_{60}$ and (d) LBSO ETLs.

factor (FF) was 85.70%, which is not affected by the variation in ETL thickness. This maximum FF value is obtained when the absorber thickness is above 1.1 μm. This finding suggests that the use of BaSnS$_3$ in ETLs can lead to highly efficient solar cell designs, regardless of the thickness of the layers. Similar characteristics can be observed with LBSO as ETL (Fig. 9(d)). In the case of the cell designs with SnS$_2$ and C$_{60}$ as ETL, notable FF values are found in a very narrow arrangement of ETL and absorber thicknesses, which suggests their unlikely potential in the design (Fig. 9(b) and (c)), respectively.

Through the contour plots presented in Fig. 10(a–d), we demonstrate the impact of altering the thickness of the absorber layer and ETL on the power conversion efficiency (PCE) of various solar cell designs. The examination of the contour plot of power conversion efficiency (PCE) for four separate ETL-based solar configurations shows that each material possesses a unique set of features. The structure with ITO/ZnS/BaSnS$_3$/Pt (Fig. 10(a)) showcases a wide high-efficiency area, with the peak value reaching 26.08% as the absorber thickness increased above 1.1 μm. In the case of optimal power conversion efficiency, the ITO/ZnS/BaSnS$_3$/Pt structure

(Fig. 10(a)) demonstrates a more localized high-efficiency region, emphasizing the need for precise thickness control. The peak efficiency is achieved regardless of the variation in the ETL thickness. In the case of SnS$_2$ as ETL, the maximum PCE of 26.05% is found when the absorber thickness is above 1.1 μm (Fig. 10(b)). In the case of the C$_{60}$-based cell design, the lowest value of 25.62% is found when the absorber thickness is above 0.8 μm and the ETL thickness is within 0.045 μm (Fig. 10(c)). Lastly, the LBSO ETL-based structure mirrors the extensive efficiency of ZnS. The PCE value for the ITO/LBSO/BaSnS$_3$/Pt-based structure is 25.89% (Fig. 10(d)). A consistent absorber thickness of around 1.0 μm is linked to a high power conversion efficiency (PCE) across all configurations, underscoring its importance in the solar cell design. The range of optimal ETL thicknesses is not concerning given that it has little to no effect on the overall performance of all the configurations. In conclusion, the ITO/ZnS/BaSnS$_3$/Pt design with an absorber thickness of 1.0 μm is shown to provide the maximum performance with optimized layer thickness. In the simulation, the peak efficiency was observed to remain nearly constant across a range of ETL thicknesses. This is because other parameters
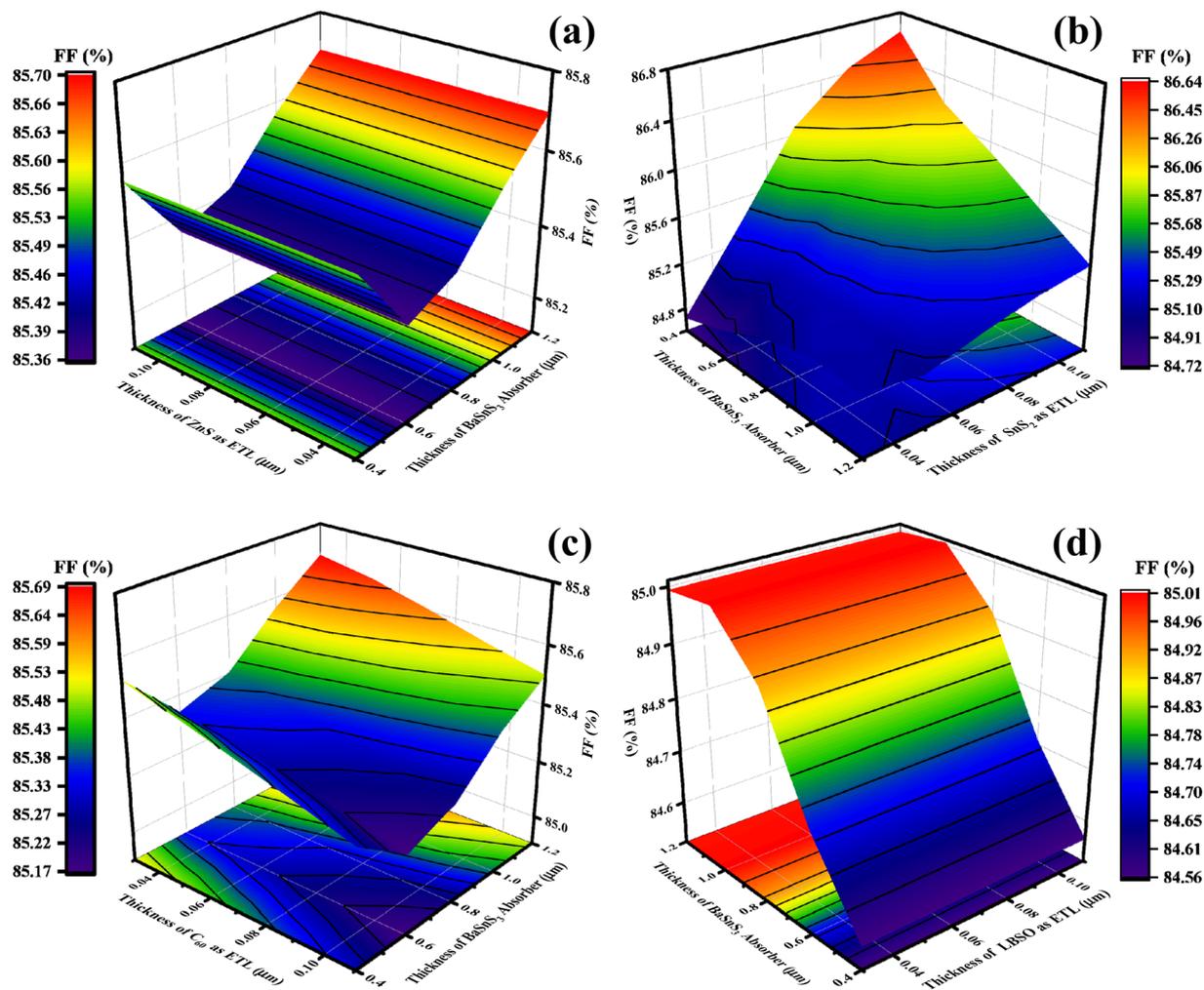
Fig. 9 Contour mapping of FF (%) with (a) ZnS, (b) SnS$_2$, (c) C$_{60}$, and (d) LBSO ETLs.

such as absorber thickness, defect density, and mobility were fixed, and the simulated ETL thickness variation (typically in the range of tens to a few hundred nanometers) did not introduce significant resistive or optical losses. However, it is noted that in real solar cell fabrication, changes in the ETL thickness may affect the film morphology, resistance, and light management, which could influence the efficiency outcomes more significantly than in the idealized simulation environment.

3.2.4 Influence of changing absorber thickness. The absorber thickness plays a crucial role in the overall performance of solar cells. It is directly linked with the production cost of the cell. The target is to achieve the maximum performance output with minimum production cost. Using a very thin layer of absorber may lower the production cost, but will result in a poor cell performance. Similarly, using a very thick layer may generate a higher output, but has a risk of increased chance of recombination as well as high production cost. Hence, the change in absorber thickness is sensitive and needs to be properly optimized for achieving the best performance. To efficiently harvest energy, a solar cell needs to be thick enough so that the charge carriers it generates do not disperse before

being collected. It is important to maintain a balance between how much light is absorbed and how many charge carriers (electrons and holes) recombine. Typically, the thickness of the absorber layer plays a key role in directing these carriers toward the electron transport layers (ETLs) and ensuring effective energy conversion. Because a thicker layer absorbs more light, it can enhance the functionality of the gadget. The analysis of the BaSnS$_3$-based solar cell with different ETLs showed that the ITO/ZnS/BaSnS$_3$/Pt configuration has the best performance overall. Now, to get the optimized absorber thickness for the above-mentioned configuration, the thickness of the absorber was varied from 0.4 μm to 1.2 μm and the performance was observed for all the solar cell configurations. The simulation results are depicted in Fig. 11(a–d).

Fig. 11(a) shows the change in V_{OC} as the absorber thickness is varied for different ETLs. The analysis shows that the relation between absorber thickness and V_{OC} is inversely proportional. This tendency occurs due to the inverse saturation current.[77] As seen in Fig. 11(a), the maximum V_{OC} is obtained at 0.4 μm for all the ETLs except C$_{60}$. However, as the thickness increases, gradual decline is observed for all the cell configurations. At 1.2
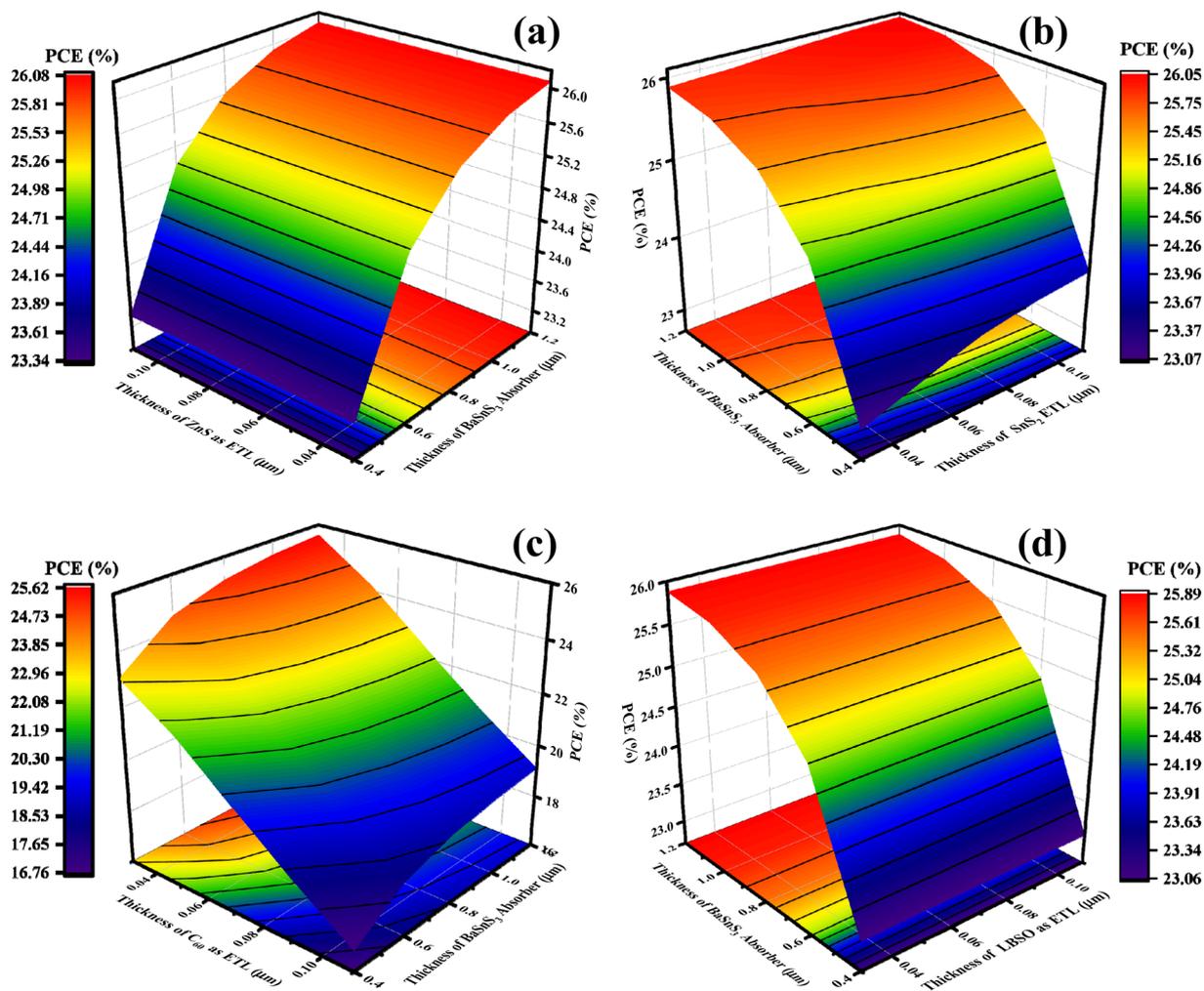
Fig. 10 Contour mapping of PCE (%) with (a) ZnS, (b) SnS$_2$, (c) C$_{60}$, and (d) LBSO ETLs.

μm, the V_{OC} dropped to 1.13 V essentially for all the ETLs. ZnS, SnS$_2$ and LBSO showed similar responses, with SnS$_2$ having slightly better output, while C$_{60}$ performed the lowest.

The current density of a solar cell increases as the thickness of the absorber increased. This happens due to the high spectral response at longer wavelength with an increment in the absorber thickness.[78] The expected output curve is seen in Fig. 11(b) for all the combinations. All ETLs the except C$_{60}$ have a similar response of around 23.2 mA cm^{-2} at 0.4 μm to 26.94 mA cm^{-2} at 1.2 μm. In the case of C$_{60}$, the value of J_{SC} increased from 21.64 mA cm^{-2} to 25.08 mA cm^{-2} with a variation in absorber thickness from 0.4 μm to 1.2 μm.

Fig. 11(c) shows the change in FF across different absorber thicknesses for different ETL configurations, where the trend in the plot is interesting. In the case of ZnS, SnS$_2$ and C$_{60}$, the value of FF decreases with an increment in thickness from 0.4 μm to 0.6 μm. From that point onwards, ZnS and C$_{60}$ maintained a similar upward trend with a slight variation in the FF values as the thickness increased. SnS$_2$ maintained a steady trend as the thickness reached 0.8 μm, and eventually the FF decreased as the thickness reached 1.2 μm. In the case of LBSO, a steady

increase in FF was seen from 0.4 μm to 1.0 μm and it remained pretty much the same for 1.0 μm and 1.2 μm.

With an increase in absorber thickness, more photons can be absorbed, and thus more energy can be harnessed. This results in high efficiency, which is proven by the variation in PCE for different ETL configurations across various absorber thicknesses, shown in Fig. 11(d). All the ETLs showed a similar trend, with ZnS, SnS$_2$ and LBSO performing pretty close to each other. ZnS had the maximum PCE at both low (23.34% at 0.4 μm) and high thickness (26.08% at 1.2 μm) among the ETLs. The worst variation in PCE is observed for C$_{60}$ with a change in absorber thickness (21.73% at 0.4 μm and 24.20% at 1.2 μm). The analysis of the cell performance based on absorber thickness suggests that the best-performing ETL is ZnS, while the optimized absorber thickness is 1.0 μm.

3.2.5 Influence of changing absorber defect density (N_t). A solar cell absorber performs best when it is pure. Any type of defect induces performance issues in the cell. Theoretically, it is easy to analyze the performance of a solar cell when considering that all the layers are free from defects. However, in practical scenarios, the absorber may contain defects, which will affect its
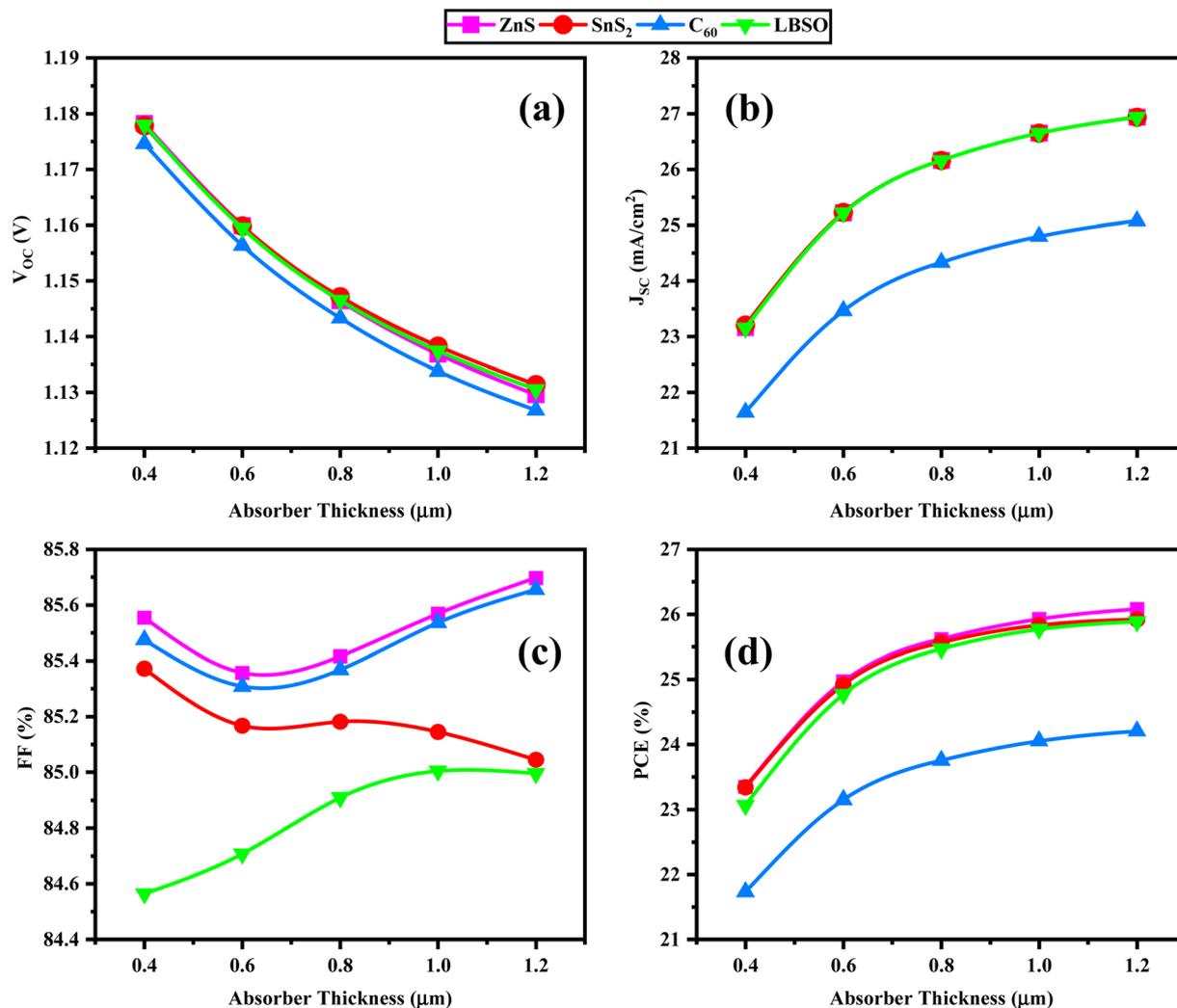
Fig. 11 Effect of absorber thickness on performance parameters of (a) V_{OC}, (b) J_{SC}, (c) FF, and (d) PCE of (ITO/ETL/BaSnS$_3$/Pt); ETL = ZnS, SnS$_2$, C$_{60}$ and LBSO.

overall performance. Given that the absorber layer is primarily responsible for generating electricity, its quality is crucial for harnessing the maximum output. Defects in this layer can cause serious issues such as instability, rise in recombination and overall degradation of the cell structure.[79] Furthermore, they cause mismatch in the band alignment between the absorber layer and ETL layer, which results in an underwhelming output performance.[80,81] In an attempt to analyze the effect of the absorber density on V_{OC}, J_{SC}, FF and PCE, a theoretical approach based on the Shockley–Read–Hall model is examined. This model consists of the following equations:[82,83]

$$\tau_{n,p} = \frac{1}{\sigma v_{th,n,p} N_t} \tag{8}$$

$$R_{SRH} = \frac{np - n_i^2}{\tau_{p(n+n_i)} + \tau_n(p + p_i)} \tag{9}$$

The position and depth of a defect determine whether it is considered shallow or deep. Typically, shallow defects have

a density in the range of 10^{10} to 10^{13} cm^{-3}, while deep defects can have a density of around 10^{14} cm^{-3}, potentially reaching up to 10^{16} cm^{-3}.[84] When the number of defects in the absorber layer increases, the Shockley–Read–Hall model predicts that the quality of the stacked materials will deteriorate, leading to the generation of recombinants and a reduced carrier lifetime. The observed consistent and significant decline in V_{OC}, J_{SC}, FF, and PCE with an increase in absorber defect density (Fig. 12(a–d)) across all the investigated ETLs strongly indicates that the defect density in the absorber layer is the paramount limiting factor in the device performance over the varied range (10^{15} to 10^{19} cm^{-3}). The physical mechanisms underpinning these trends stem from fundamental processes of charge carrier generation, transport, and recombination within the solar cell. The open-circuit voltage (V_{OC}) is directly linked to the separation of quasi-Fermi levels within the absorber under illumination. As the defect density (N_t) increases, a greater number of recombination centres are introduced within the BaSnS$_3$ material. This increased recombination reduces the carrier lifetime, diminishing the quasi-Fermi level splitting, and
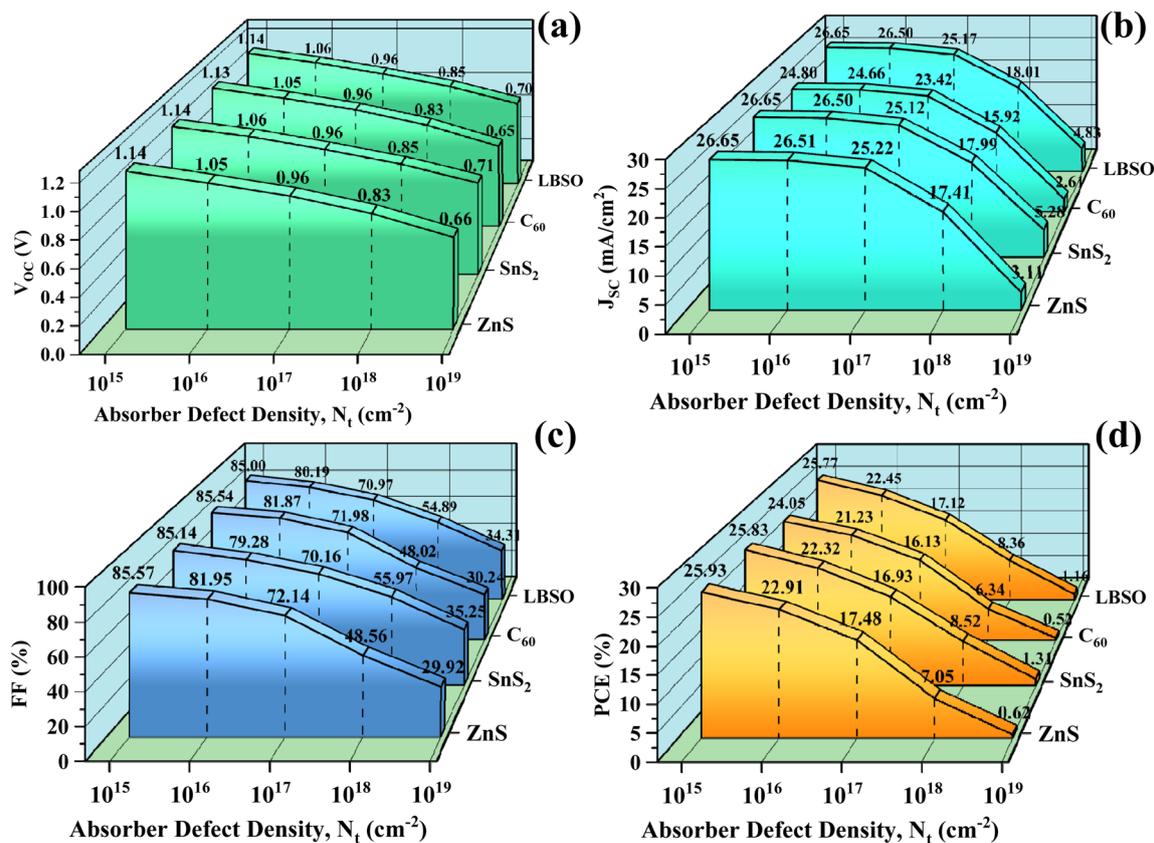
Fig. 12 Effect of absorber defect density on performance parameters of (a) V_{OC}, (b) J_{SC}, (c) FF, and (d) PCE of (ITO/ETL/BaSnS$_3$/Pt); ETL = ZnS, SnS$_2$, C$_{60}$ and LBSO.

consequently causing a sharp decrease in V_{OC} for all the ETLs, as seen in Fig. 12(a). Similarly, the short-circuit current density (J_{SC}), determined by the collection of photogenerated carriers, experiences a decline because the enhanced recombination losses within the absorber prevent a larger fraction of carriers from reaching the electrodes. Although the initial J_{SC} values may be stable at lower defect densities, beyond a critical threshold such as 10^{17} cm^{-3}, recombination severely limits the carrier collection, leading to a noticeable drop in J_{SC} given that fewer carriers contribute to the external current, as seen in Fig. 12(b). The fill factor (FF), which reflects the squareness of the J–V curve and charge extraction efficiency, also deteriorates significantly with an increase in absorber defect density. This degradation is due to the increased recombination, particularly under a forward bias, and potentially to trap-assisted tunnelling or shunting pathways that cause current leakage. Given that these defects are inherent in the absorber material, their detrimental impact on the J–V curve shape and current output is largely independent of the specific ETL, explaining the consistent FF degradation seen in Fig. 12(c). Consequently, given that the V_{OC}, J_{SC}, and FF all decline with an increase in the absorber defect density, their combined effect results in a sharp and substantial reduction in the overall power conversion efficiency (PCE). This profound inverse relationship between defect density and PCE underscores that achieving high-quality, defect-free BaSnS$_3$ absorber layers is critical for maximizing

the performance of these devices, given that the optimal performance is observed at a defect density of 10^{15} cm^{-3}.

3.2.6 Effect of series resistance (R_S). The series resistance (R_S) and shunt resistance (R_{sh}) are critical parameters that significantly influence the performance of photovoltaic (PV) cells. R_S arises from the inherent resistive components within the device, including the semiconductor layers and metal contacts, which impede current flow and reduce the overall efficiency. In contrast, R_{sh} is associated with the unintended leakage pathways that allow the current to bypass the active region, thereby diminishing the device performance. An increase in R_S typically leads to a reduction in fill factor (FF), which can also lower the short-circuit current density (J_{SC}) and overall power conversion efficiency (PCE). Conversely, a decrease in R_{sh} results in a reduced open-circuit voltage (V_{OC}) and FF, further compromising the PCE. The simultaneous presence of high R_S and low R_{sh} can severely degrade the device efficiency, emphasizing the importance of optimizing both parameters during fabrication. Ideally, achieving low R_S and high R_{sh} is essential for maximizing the performance of PV cells. To showcase the effects of R_S and R_{Sh} on the top four solar structures, the value of R_S was adjusted from 0 to 6 Ω cm^2, while keeping R_{sh} constant at 10^5 Ω cm^2 (Fig. 13(a–d)). A decrease in the FF and PCE values of all four solar configurations is observed as R_S increases. However, the J_{SC} and V_{OC} values for all the structures remained consistent as R_S increased. All the ETLs
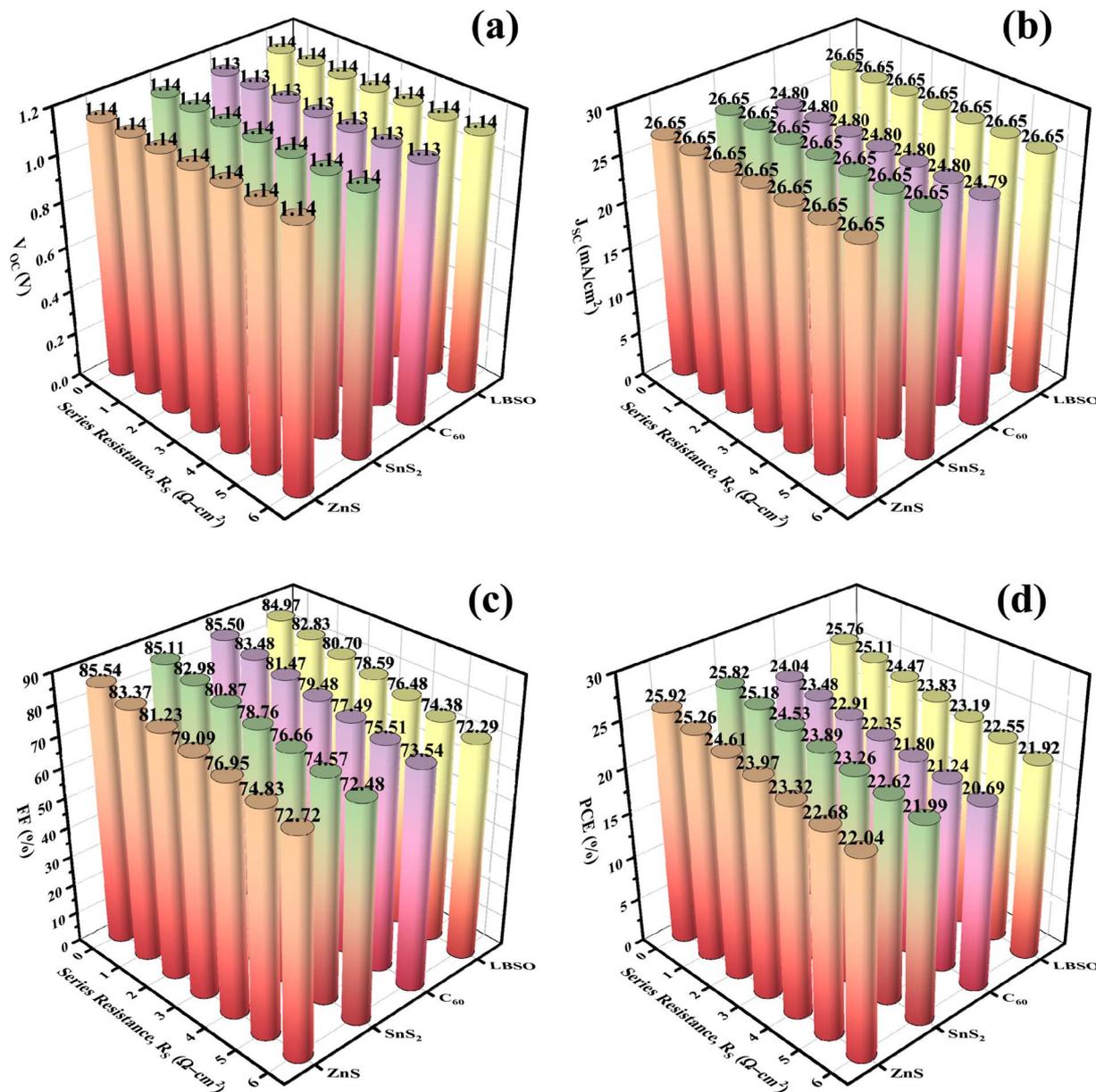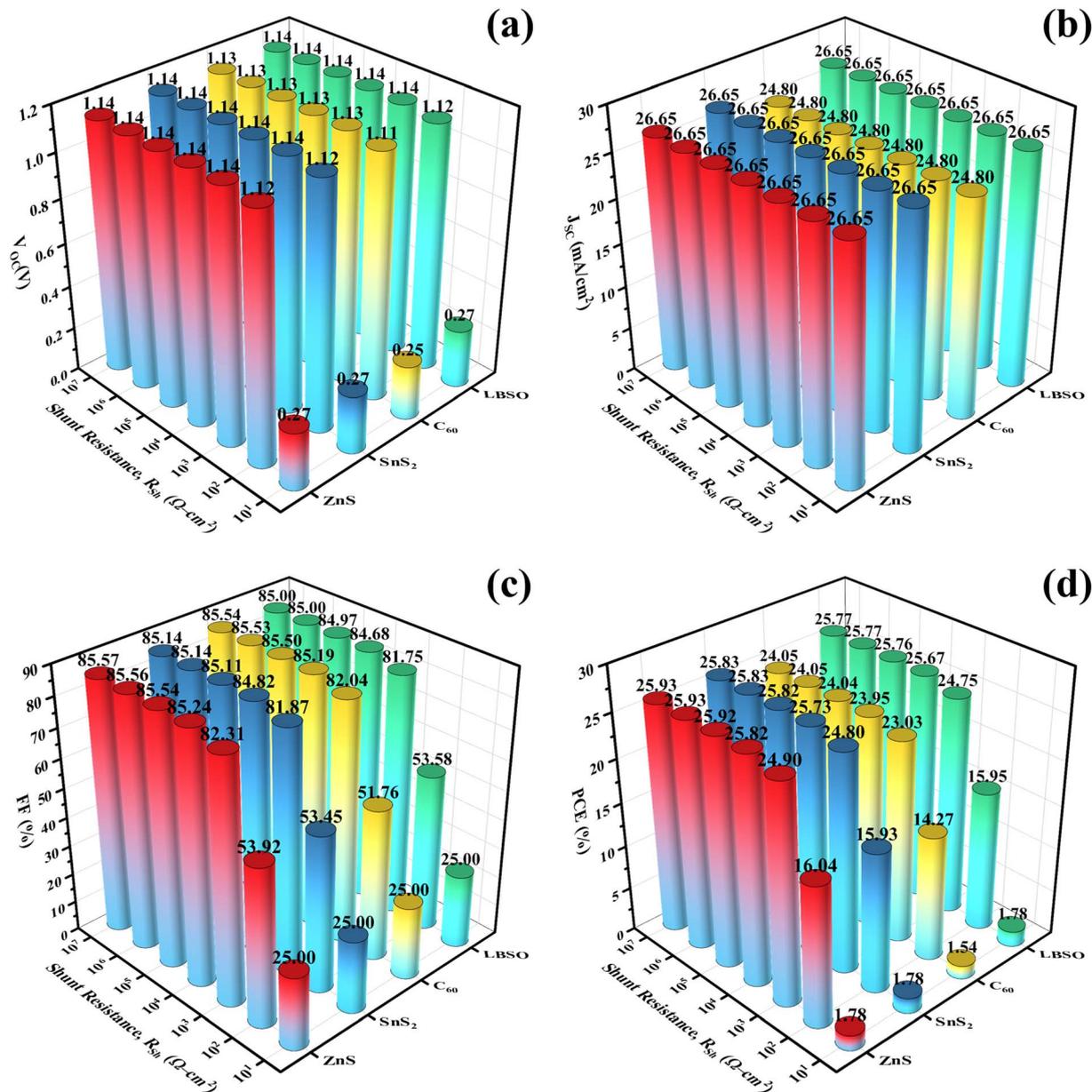
Fig. 13 Effect of series resistance, R_S, on the performance parameters of (a) V_{OC}, (b) J_{SC}, (c) FF, and (d) PCE of (ITO/ETL/BaSnS$_3$/Pt); ETL = ZnS, SnS$_2$, C$_{60}$ and LBSO.

except the C$_{60}$-based structure exhibited the highest J_{SC} and V_{OC}. Among the top four solar structures, the ZnS and C$_{60}$ ETL configurations achieved the highest FF values of approximately 85.5%, respectively (Fig. 13(c)). In the case of the PCE, the ZnS, SnS$_2$ and LBSO ETLs showed the maximum efficiency of around 25.9% (Fig. 13(d)). However, as R_S increased, both the PCE and FF values decreased to around 22% and 72%, respectively. The V_{OC} and J_{SC} values for the four optimized SCs remain constant as R_S increased, indicating that R_S does not affect these performance parameters (Fig. 13(a and b)), respectively. The ZnS, SnS$_2$ and LBSO ETL-based solar structures consistently exhibited the highest J_{SC}, approximately 26.65 mA cm^{-2} (Fig. 13(b)), and all the ETLs except C$_{60}$ show the highest V_{OC} values, reaching approximately 1.14 V, regardless of their R_S

values (Fig. 13(a)). An ITO layer with high conductivity has a minimal impact on R_S, while a nonohmic contact in a PSC shows a significant R_S. The resistance at the junction of semiconductors and metal contacts plays a significant role in the R_S of an SC. FF decreases significantly when the R_S increases, resulting in a decrease in PCE due to the increased power loss. As a result, FF and PCE show a significant decrease as R_S increases, as shown by the simulation results.

3.2.7 Effect of shunt resistance (R_{sh}). Generally, shunt resistance occurs in solar cells due to recombination leakage channels and photoactive layers. Fig. 14(a–d) illustrate the impact of varying R_{sh} on the output parameters of the ITO/ETL/BaSnS$_3$/Pt SC, including V_{OC}, J_{SC}, FF, and PCE. In this study, R_{sh} varied from 10^1 to 10^7 Ω cm^2, while R_S remained constant at 0.5

Fig. 14 Effect of shunt resistance, R_{sh}, on the performance parameters of (a) V_{OC}, (b) J_{SC}, (c) FF, and (d) PCE of (ITO/ETL/BaSnS$_3$/Pt); ETL = ZnS, SnS$_2$, C$_{60}$ and LBSO.

Ω cm^2. According to Fig. 14(a–d), it can be observed that the V_{OC}, FF, and PCE values showed an increase as R_{sh} increased from 10^1 to 10^3 Ω cm^2. From 10^3 Ω cm^2, the values remained unchanged for higher values of R_{sh} (Fig. 14(a), (c) and (d)). Conversely, the J_{SC} remained constant in all the structures (Fig. 14(b)). The ZnS, SnS$_2$ and LBSO ETL-based solar structures have identical high J_{SC}, which is about 26.65 mA cm^{-2} (Fig. 14(b)). As the R_{sh} for all the device configurations increased, the FF and PCE showed an average increase of 82.31% and 24.9% at 10^3 Ω cm^2 (Fig. 14(c) and (d)), respectively. Beyond that point, they remained at their maximum value of > 85% FF and > 25% PCE. The manufacturing defects of solar cells contribute to an increase in R_{sh}.[85] This study demonstrates

that by varying R_{sh}, the performance parameters of solar cells can be greatly optimized. Increasing R_{sh} can enhance the device performance, given that it facilitates a pathway with low resistance, enabling the junction to flow more freely.[86] To create a highly effective device, it is important to achieve a low series resistance and a high shunt resistance. Eqn (10) has been written for the ideal single-diode device to provide a better understanding of R_{sh} and R_S.[87]

$$I = I_L - I_0 \left[\exp\left(\frac{q(M)}{Ak_BT} \right) - 1 \right] - \left(\frac{M}{R_{sh}} \right) \tag{10}$$

In this equation, M is equal to V plus the product of I and R_S. A represents the ideality factor, k_B stands for the Boltzmann

constant, T represents the temperature, and q represents the charge of an electron. The I_L represents the current generated by light, while I_0 refers to the reverse saturation current of the diode. Eqn (11) and (12) depict the equations for R_S and R_{sh}, respectively, derived from the J–V curves. Here, ΔV represents the variation in voltage and ΔI represents the variation in current.

$$R_{sh} = -\frac{\Delta V}{\Delta I}(V = 0) \tag{11}$$

$$R_s = -\frac{\Delta V}{\Delta I}(V = V_{oc}) \tag{12}$$

3.2.8 Effect of temperature (T). In previous simulation studies, an initial temperature of 300 K was typically assumed. However, given that solar cells operate in outdoor environments, their performance is inherently influenced by temperature fluctuations. Therefore, it is essential to evaluate the impact of temperature variations on the efficiency of contemporary solar cell (SC) technologies. To investigate this effect, simulations were conducted over the temperature range of 300

K to 450 K under constant illumination of 1000 W m^{-2}. The resulting device characteristics are illustrated in Fig. 15(a–d), which collectively indicate a decline in performance with an increase in temperature. Notably, the open-circuit voltage (V_{OC}) decreases significantly from 1.14 V to 0.87 V across all device configurations (Fig. 15(a)). This reduction is attributed to the temperature-dependent narrowing of the band gap of the material. With an increase in temperature, the bandgap of semiconductors typically narrows due to the enhanced electron–phonon interactions and lattice expansion effects. Phonon-induced perturbations reduce the energy separation between the valence and conduction bands, while thermal expansion increases the interatomic spacing, which modifies the orbital overlap and further reduces the bandgap. This behavior is observed in many semiconducting materials and is consistent with theoretical predictions and experimental results reported in the literature.[88–90] Additionally, a temperature-induced increase in short-circuit current density (J_{SC}) is observed for the C$_{60}$-based electron transport layer (ETL), while J_{SC} remains relatively stable for the devices incorporating alternative ETLs (Fig. 15(b)). This distinct behavior for C$_{60}$ can
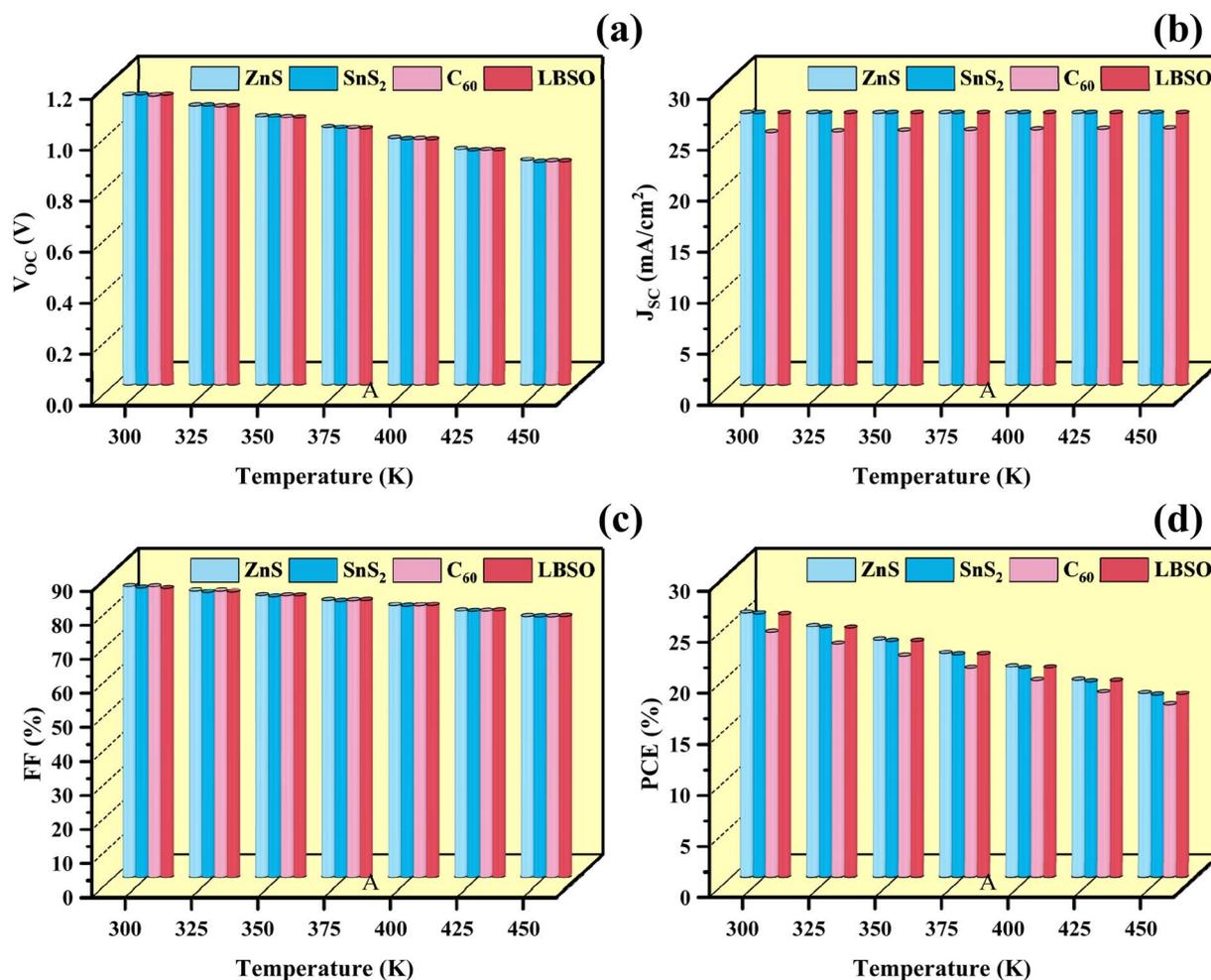

Fig. 15 Effect of temperature on the performance parameters of (a) V_{OC}, (b) J_{SC}, (c) FF, and (d) PCE of (ITO/ETL/BaSnS$_3$/Pt); ETL = ZnS, SnS$_2$, C$_{60}$ and LBSO.

be attributed to a combination of factors related to its organic semiconductor nature and how these properties interact with temperature. Unlike inorganic ETLs such as ZnS, SnS$_2$, and LBSO, where charge transport is predominantly band-like, charge transport in organic semiconductors such as C$_{60}$ often involves hopping mechanisms. In some organic materials, the carrier mobilities can exhibit a positive dependence on temperature within a certain range due to the enhanced phonon-assisted hopping.[91] The slight increase in electron mobility in C$_{60}$ with an increase in temperature could lead to more efficient collection of photogenerated carriers, thereby boosting J_{SC}. Furthermore, subtle temperature-induced shifts in the E_C and E_V energy levels and their alignment at the C$_{60}$/BaSnS$_3$ interface (as depicted in Fig. 6(c)) could favor more efficient electron extraction as the temperature rises. Even minor changes in band alignment can improve the driving force for charge separation and transport, contributing to an increase in J_{SC}. Additionally, C$_{60}$ has the lowest bandgap (1.7 eV) among the investigated ETLs, as seen in Table 1. Although ETLs are primarily for charge transport, a lower bandgap can influence the temperature-dependent absorption characteristics. As the temperature increases, the effective bandgap of all the materials generally narrows.[92] In the case of C$_{60}$, this bandgap narrowing might lead to a relatively larger increase in the absorption of photons, particularly those closer to its absorption edge, contributing to more photogenerated carriers, and thus higher J_{SC}. Lastly, the behavior of defects, especially at the interfaces, is highly temperature dependent. It is plausible that certain defect states within the C$_{60}$ layer or at the C$_{60}$/BaSnS$_3$ interface become less active as recombination centres with an increase in temperature. This could lead to a reduction in non-radiative recombination losses, effectively increasing the number of collected charge carriers, and consequently J_{SC}. This complex interplay between material characteristics, temperature, and device physics is particularly evident in hybrid and organic solar cell systems. A temperature-induced increase in J_{SC} is observed for the device incorporating C$_{60}$ as the ETL, whereas J_{SC} remains relatively stable for the devices employing alternative ETLs such as ZnS, SnS$_2$, and LBSO. This variation is not due to the ETL itself, but rather the overall device behavior influenced by the ETL-absorber interface. Other ETLs may form more stable or less temperature-sensitive interfaces, resulting in minimal change in current output with temperature. Elevated operating temperatures also adversely affect both the power conversion efficiency (PCE) and fill factor (FF), primarily due to their influence on the band gap, charge carrier concentration, and carrier mobility, which are factors that collectively degrade the overall performance of perovskite solar cells (Fig. 15(c) and (d)),
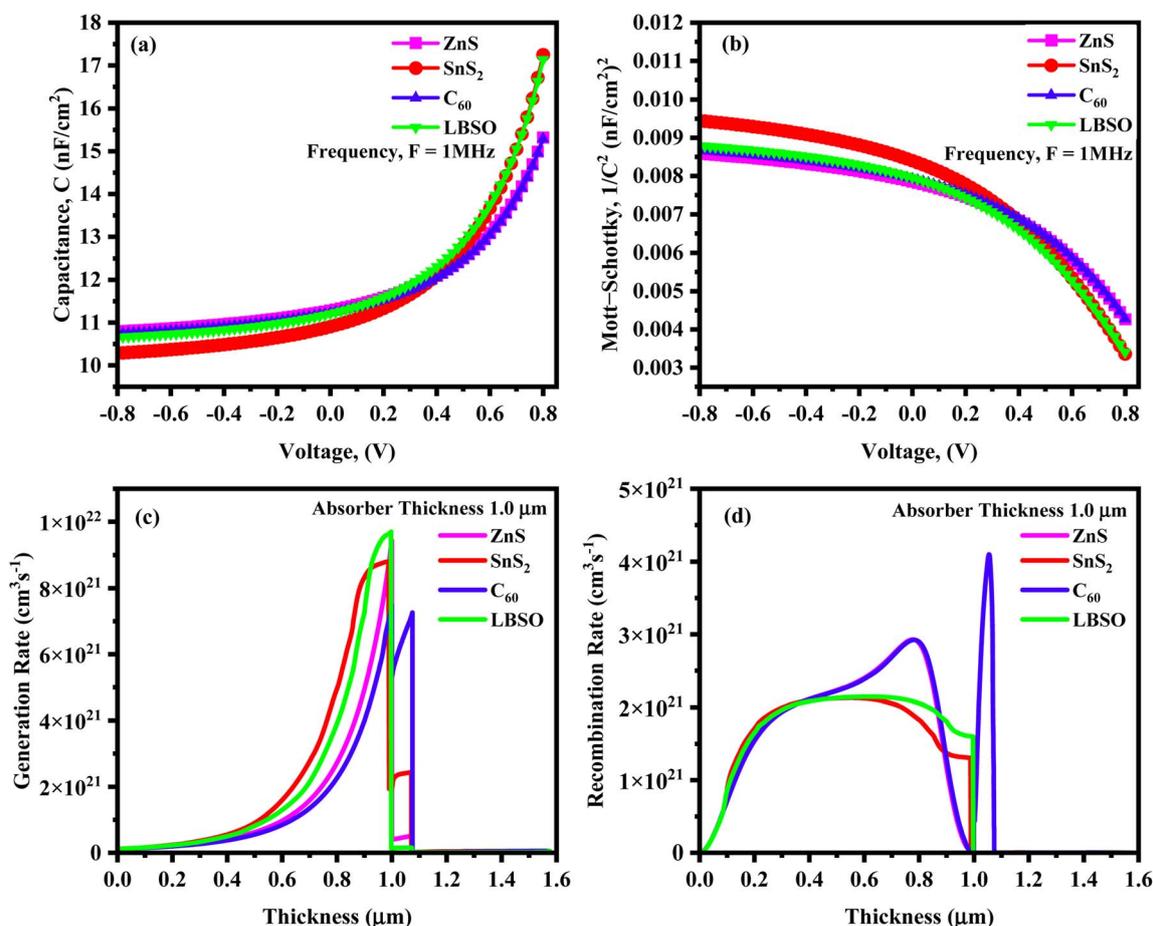

Fig. 16 (a) Capacitance (C), (b) Mott–Schottky (1/C^2), (c) generation rate, and (d) recombination rate for the four studied structures.

respectively. These findings reveal an approximately linear inverse relationship between temperature and device efficiency, with lower temperatures yielding a superior performance.

3.2.9 Effect of capacitance and Mott–Schottky. Fig. 16(a and b) show the output curves of capacitance per unit area (C) and Mott–Schottky (M–S) when a bias voltage (V) is employed. The analysis is conducted in such a way that the bias voltage alters between −0.8 to 0.8 at a fixed frequency of 1 MHz. Fig. 16(a) shows that the capacitance per unit area increases exponentially with an increment in voltage from around 0.2 V. The maximum capacitance per unit area obtained for the SnS_2 and LBSO-based configurations is 17.25C and 17.14C, respectively. The ZnS- and C_{60}-based configurations achieved the maximum capacitance of 15.32C and 15.29C, respectively. It is noteworthy to mention that the capacitance varies with a change in voltage due to the fact that the current generated at low voltage remains below the saturation current.[93]

Built-in voltage of a solar cell can be determined and analyzed through Mott–Schottky analysis. Fig. 16(b) shows the Mott–Schottky curves for all the configurations. Which exponentially decrease in the range of −0.8 V to 0.8 V. The SnS_2-based configuration has the highest Mott–Schottky value of 9.45×10^{-3} $1/C^2$ and the ZnS-based configuration has the lowest Mott–Schottky value of 8.58×10^{-3} $1/C^2$.

3.2.10 Effect of generation and recombination. Fig. 16(c and d) display how charge carriers are generated and recombined at different positions within the device structures, respectively. During this process, electrons move from the valence band (VB) to the conduction band (CB), leaving behind holes and forming electron–hole pairs. This effect is especially noticeable in $BaSnS_3$, where the movement of both electrons and holes leads to a higher number of generated carriers. In all the devices, the generation rate is lowest near 0.0001 μm and highest around 1 μm, highlighting how light absorption varies across the device layers. These differences are mainly due to how much light different regions of the device can absorb. The generation rate, $G(x)$, is calculated based on these variations, and SCAPS-1D simulates the creation of electron–hole pairs by analyzing how incoming photons interact with the layers.

3.2.11 J–V and QE characteristics. Perovskite solar cells (PSCs) have emerged as promising solar technology due to their remarkable power conversion efficiency and low production costs. To evaluate their performance, two essential parameters are typically examined, the current density–voltage (J–V) characteristics and quantum efficiency (Q-E) response. The open-circuit voltage (V_{OC}) represents the maximum voltage the cell can deliver when no current flows, while the short-circuit current density (J_{SC}) indicates the maximum current generated under illumination when the voltage is zero. Alternatively, the quantum efficiency measures how effectively the cell converts incident photons into collected charge carriers, providing insight into the responsiveness of the cell across the solar spectrum. The wavelength-dependent behavior of Q-E reveals the spectral utilization of the device and identifies losses from transmission, reflection, and non-radiative recombination, which are critical factors for further design optimization.

Fig. 17(a and b) present the J–V and Q-E profiles for all the devices, respectively. Each device exhibited a current density of zero at V_{OC} value of 1.17 V. As shown in Fig. 17(a), the current density consistently decreases with an increase in voltage, aligning with established trends in photovoltaic behavior. The Q-E spectra in Fig. 17(b) span wavelengths from 300 nm to 900 nm. Initially, the Q-E values start around 98%, peak near 100%, and then gradually decline to zero at around 800 nm for all the designs except the C_{60}-based design. In the case of the C_{60}-based design, its initial QE value was 50%, which reached the peak of around 92% at 720 nm, and eventually reached zero at 800 nm. This decline in Q-E at higher wavelengths corresponds well with the patterns observed in the J–V characteristics. It is noted that the quantum efficiency (QE) at 300 nm in the simulation reaches up to ∼98%, which is significantly higher than the typical experimental values. This result arises due to the idealized nature of SCAPS-1D simulations, where UV-induced degradation, interface recombination, and parasitic absorption in the ETL or TCO layers are not explicitly modeled unless additional parameters are introduced. In real devices, the QE at short wavelengths is generally suppressed by these non-ideal effects.
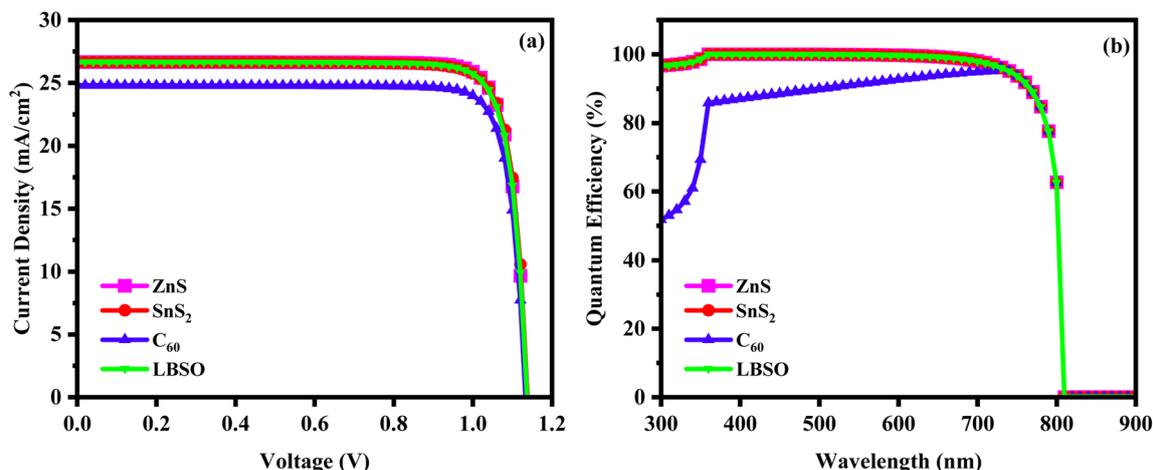

Fig. 17 (a) J–V characteristics and (b) QE curves of the PSCs.

Table 3 Comparison of PV parameters of BaSnS$_3$-based solar cells

Structure	V_{OC} (V)	J_{SC} (mA cm^{-2})	FF (%)	PCE (%)	Ref.
ITO/ZnS/BaSnS$_3$/Pt	1.136	26.65	85.57	25.93	This work
ITO/SnS$_2$/BaSnS$_3$/Pt	1.138	26.65	85.14	25.83	This work
ITO/C$_{60}$/BaSnS$_3$/Pt	1.133	24.79	85.54	24.05	This work
ITO/LBSO/BaSnS$_3$/Pt	1.137	26.65	85	25.77	This work
FTO/TiO$_2$/BaZrS$_3$/CZTS/Au	1.04	28.39	71.92	21.24	94
ITO/ZnO/CsSnCl$_3$/CBTS/Au	1.01	26.22	81.93	21.72	95
FTO/ZnO/KSnI$_3$/CuI/Au	1.44	17.06	85.24	20.99	96
FTO/ZnO/CH$_3$NH$_3$SnI$_3$/Cu$_2$O/Au	1.03	30.14	85.58	26.55	97
FTO/ZnO/MAPbI$_3$/LNMO/Cu$_2$O/Au	0.23	2.05	50.03	24.01	98
ITO/PCBM/CsSnI$_3$/CFTS/Se	0.87	33.99	83.46	24.73	99
FTO/TiO$_2$/BaZrSe$_3$/Spiro-OMeTAD/Au	0.71	35.68	77.78	19.71	100
AZO/ZnS/SrZrS$_3$/a-Si:H	0.93	26.58	81.04	20.1	101

3.2.12 Comparison with SCAPS 1D results and previous studies. Table 3 summarizes the optimized performance results of the BaSnS$_3$-based ITO/ETL/BaSnS$_3$/Pt solar cells simulated using SCAPS-1D, employing four different electron transport layers (ETLs). According to the structural parameters listed in Table 1, the thickness, carrier concentration, and bulk defect density of the BaSnS$_3$ absorber were optimized at 1000 nm, 10^{15} cm^{-3}, and 10^{15} cm^{-3}, respectively. In the ZnS, SnS$_2$, C$_{60}$ and LBSO ETLs, the thickness was set 50 nm, the carrier concentration ranged from 10^{16} to 2×10^{21} cm^{-3}, and the defect density was maintained at 10^{15} cm^{-3}. Following the optimization process, the simulated power conversion efficiencies (PCEs) for the solar cells were recorded as 25.93%, 25.83%, 24.05%, and 25.77% for the devices incorporating ZnS, SnS$_2$, C$_{60}$ and LBSO as the ETL, respectively. Through a literature review, it is concluded that no previous solar cell performance analysis has been performed on BaSnS$_3$-based solar cell gadgets. As a result, the performance output of this study is compared with similar structured chalcogenide compounds and other contemporary cell designs and listed in Table 3. The device structure presented in Table 3 demonstrates significantly enhanced efficiency compared to previously reported solar cells. Other reported structures featuring the same structured BaZrS$_3$ absorber have achieved efficiencies ranging from 17.90% to 21.99%, but these configurations generally exhibit lower J_{SC} values than that in the current investigation. This improvement can be attributed to the adjustments in absorber characteristics, such as thickness and defect density, as well as the unique combination of ETLs and HTLs used, which differ from previously published theoretical models. Furthermore, the differences in optical properties across the absorbers influence the solar energy absorption capabilities. The superior optical behavior of the BaSnS$_3$ absorber used here likely contributes to the enhanced PCE, reinforcing the conclusion that the simulated structures presented in this study outperform earlier Sn-based and similar perovskite solar cell designs.

4 Limitation

Although our study is purely computational and simulation based, it is recognized that the experimental realization of BaSnS$_3$ remains challenging. The only available reports on BaSnS$_3$ date back to its bulk synthesis under high-pressure conditions in the 1970s, where the perovskite phase was obtained using a piston-cylinder apparatus at several gigapascals pressure.[102] More recent work by researchers confirms that Ba–Sn–S contains numerous competing phases, making its phase purity and stoichiometry control particularly tricky in standard ambient-pressure synthesis.[103] Although there are no current reports of thin-film BaSnS$_3$, synthesis studies on related chalcogenide perovskites such as BaZrS$_3$ (ref. 104) suggest possible routes including solid–state reactions with BaS and ZrS$_2$, sulfurization of oxide precursors, and pulsed-laser deposition, followed by sulfur dosing at elevated temperatures (500–1000 °C). Translating these methods to BaSnS$_3$ would require careful optimization to avoid competing phases such as Ba$_3$Sn$_2$S$_7$, Ba$_2$SnS$_4$, and BaSn$_2$S$_3$ containing non-perovskite structures.[105] Thin-film formation poses additional challenges such as maintaining the sulfur stoichiometry and a uniform morphology, especially for Sn^{2+} chemistry, which may benefit from sulfur-rich atmospheres or advanced deposition strategies such as sulfur plasma-assisted growth or chemical vapor transport, remaining unexplored for BaSnS$_3$. Despite these hurdles, it is believed that the demonstrated thermal and chemical stability of analogous chalcogenide perovskites supports the potential for the future experimental realization of BaSnS$_3$ solar absorbers, especially leveraging emerging deposition methods recently seen in BaZrS$_3$ and BaHfS$_3$ systems.[106] Furthermore, given that this work is entirely theoretical and based on simulation, it does not account for degradation mechanisms under environmental stressors such as humidity, oxygen, and photochemical instability. However, we have investigated the effect of temperature variation on the device output parameters, which provides insight into thermal behavior under operational conditions. The simulated results show that the efficiency decreases with an increase in temperature, mainly due to the increased recombination and decreased V_{OC}. The BaSnS$_3$-based device retains a significant portion of its performance across a broad temperature range. This suggests that this architecture may offer a degree of thermal resilience. Nonetheless, experimental studies will be necessary to evaluate its long-term stability under real-world environmental conditions.

5 Conclusion

This study employed first-principles density functional theory (DFT) calculations to examine the structural, electronic, and optical properties of $BaSnS_3$ and examine its capability as a solar cell absorber. The dynamic stability of the material was validated through phonon dispersion analysis, showing no imaginary frequencies near the Γ-point. $BaSnS_3$ was found to exhibit an indirect bandgap of 1.535 eV. Comprehensive optical analysis revealed favorable characteristics, highlighting the potential of $BaSnS_3$ for photovoltaic applications. In addition to the DFT analysis, the photovoltaic potential of $BaSnS_3$ was further explored using SCAPS-1D simulations. Four device configurations were considered including ITO/ZnS/$BaSnS_3$/Pt, ITO/SnS_2/$BaSnS_3$/Pt, ITO/C_{60}/$BaSnS_3$/Pt, and ITO/LBSO/$BaSnS_3$/Pt. Among them, the structure with ZnS as the ETL demonstrated the most promising performance, achieving a power conversion efficiency (PCE) of 25.93%, an open-circuit voltage (V_{OC}) of 1.1368 V, and a short-circuit current density (J_{SC}) of 26.65182 mA cm^{-2}. The absorber layer thickness was varied between 0.4 and 1.2 μm, with the optimal performance observed at 1.0 μm. The electron transport layer (ETL) thickness showed a minimal impact on the efficiency across the range of 0.03–1.1 μm; therefore, 0.05 μm was selected for further investigation. The effect of bulk defect density (N_t) on the device performance was also analyzed, spanning the range of 1×10^{15} to 1×10^{19} cm^{-3}, providing insights into the defect-tolerance behavior. Additional analyses addressed the influence of series resistance, shunt resistance, and operating temperature on the device parameters. An increase in shunt resistance led to improvements in V_{OC}, J_{SC}, FF, and PCE, whereas a higher series resistance reduced FF and PCE, while having minimal impact on V_{OC} and J_{SC}. A temperature variation from 300 K to 450 K resulted in a linear decline in V_{OC}, FF, and PCE, with J_{SC} remaining relatively stable. The investigation also included the Mott–Schottky and capacitance characteristics, along with quantum efficiency (QE) and current density–voltage (J–V) profiles, offering comprehensive insights for researchers working on single perovskite-based photovoltaic devices. These simulation outcomes can be extended to evaluate other perovskite absorber materials and can serve as a foundational reference for experimentalists aiming to fabricate high-efficiency solar cells with optimized device architectures.

Author contributions

Mohammad Yasin Hayat Khan: Investigation, methodology, data curation, conceptualization, writing original manuscript; Sayed Sahriar Hasan: Formal analysis, Software, validation, supervision, review-editing; Md. Zillur Rahman: Formal analysis, methodology, data curation, review-editing; Md. Rasheduzzaman: Formal analysis, data curation, validation, review-editing; Md. Zahid Hasan: Formal analysis, validation, supervision, review-editing.

Conflicts of interest

There is no conflict to declare.

Data availability

The authors declare that the data supporting the findings of this study are available within the article.

Acknowledgements

References

1 A. Q. Al-Shetwi, I. Zainal Abidin, K. A. Mahafzah and M. A. Hannan, Feasibility of future transition to 100% renewable energy: Recent progress, policies, challenges, and perspectives, *J. Cleaner Prod.*, 2024, 143942, DOI: **10.1016/j.jclepro.2024.143942**.

2 A. Hima, N. Lakhdar, B. Benhaoua, A. Saadoune, I. Kemerchou and F. Rogti, An optimized perovskite solar cell designs for high conversion efficiency, *Superlattices Microstruct.*, 2019, **129**, 240–246, DOI: **10.1016/j.spmi.2019.04.007**.

3 B. Rech, *et al.*, Challenges in microcrystalline silicon based solar cell technology, *Thin Solid Films*, 2006, **511–512**, 548–555, DOI: **10.1016/j.tsf.2005.12.161**.

4 X. Qin, Z. Zhao, Y. Wang, J. Wu, Q. Jiang and J. You, Recent progress in stability of perovskite solar cells, *J. Semicond.*, 2017, **38**(1), 011002, DOI: **10.1088/1674-4926/38/1/011002**.

5 I. L. Fernández, *et al.*, Lead-Free Halide Perovskite Materials and Optoelectronic Devices: Progress and Prospective, *Adv. Funct. Mater.*, 2023, **34**(6), DOI: **10.1002/adfm.202307896**.

6 S. D. Sung, *et al.*, 14.8% perovskite solar cells employing carbazole derivatives as hole transporting materials, *Chem. Commun.*, 2014, **50**(91), 14161–14163, DOI: **10.1039/c4cc06716a**.

7 A. Hima, N. Lakhdar and A. Saadoune, Effect of Electron Transporting Layer on Power Conversion Efficiency of Perovskite-Based Solar Cell: Comparative Study, *J. Nano-Electron. Phys.*, 2019, **11**(1), 01026–3, DOI: **10.21272/jnep.11(1).01026**.

8 I. Yamada, A. Takamatsu and H. Ikeno, Complementary evaluation of structure stability of perovskite oxides using bond-valence and density-functional-theory calculations, *Sci. Technol. Adv. Mater.*, 2018, **19**(1), 101–107, DOI: **10.1080/14686996.2018.1430449**.

9 M. Yang, *et al.*, Reduced Efficiency Roll-Off and Enhanced Stability in Perovskite Light-Emitting Diodes with Multiple Quantum Wells, *J. Phys. Chem. Lett.*, 2018, **9**(8), 2038–2042, DOI: **10.1021/acs.jpclett.8b00600**.

10 A. Kojima, K. Teshima, Y. Shirai and T. Miyasaka, Organometal Halide Perovskites as Visible-Light Sensitizers for Photovoltaic Cells, *J. Am. Chem. Soc.*, 2009, **131**(17), 6050–6051, DOI: **10.1021/ja809598r**.

11 National Renewable Energy Laboratory, *Best Research-Cell Efficiency Chart | Photovoltaic Research | NREL*, Nrel.gov, 2024. **https://www.nrel.gov/pv/cell-efficiency.html**.

12 Md. Z. Rahaman, Md. A. Rahman and Md. A. R. Sarker, Prediction of a new transition metal oxide $MgRhO_3$ with $SrTiO_3$-type structure: Stability, structure and physical characteristics, *Chin. J. Phys.*, 2017, **55**(4), 1489–1494, DOI: **10.1016/j.cjph.2017.03.021**.

13 B. Vargas, E. Ramos, E. Pérez-Gutiérrez, J. C. Alonso and D. Solis-Ibarra, A Direct Bandgap Copper–Antimony Halide Perovskite, *J. Am. Chem. Soc.*, 2017, **139**(27), 9116–9119, DOI: **10.1021/jacs.7b04119**.

14 T. Li, X. Wang, Y. Yan and D. B. Mitzi, Phase Stability and Electronic Structure of Prospective Sb-Based Mixed Sulfide and Iodide 3D Perovskite $(CH_3NH_3)SbSI_2$, *J. Phys. Chem. Lett.*, 2018, **9**(14), 3829–3833, DOI: **10.1021/acs.jpclett.8b01641**.

15 X. Liu, *et al.*, High-efficiency perovskite photovoltaic modules achieved *via* cesium doping, *Chem. Eng. J.*, 2021, **431**, 133713, DOI: **10.1016/j.cej.2021.133713**.

16 A. Islam Shimul, A. T. Islam, A. Ghosh, M. M. Hossain, S. A. Dipa and R. J. Ramalingam, Investigating charge transport layer flexibility for boosted performance in Lead-Free CsSnBr3-based perovskite solar cells, *Comput. Mater. Sci.*, 2025, **250**, 113701, DOI: **10.1016/j.commatsci.2025.113701**.

17 M. Rahaman, M. Hasan, R. M. Moinuddin and M. N. Islam, Numerical optimization of lead-based and lead-free absorber materials for perovskite solar cell (PSC) architectures: A SCAPS-1D simulation, *AIP Adv.*, 2024, **14**(9), DOI: **10.1063/5.0217486**.

18 A. Babayigit, A. Ethirajan, M. Muller and B. Conings, Toxicity of organometal halide perovskite solar cells, *Nat. Mater.*, 2016, **15**(3), 247–251, DOI: **10.1038/nmat4572**.

19 W. Zhang, G. E. Eperon and H. J. Snaith, Metal halide perovskites for energy applications, *Nat. Energy*, 2016, **1**(6), DOI: **10.1038/nenergy.2016.48**.

20 S. Idrissi, S. Ziti, H. Labrim and L. Bahmad, Band gaps of the solar perovskites photovoltaic $CsXCl_3$ (X=Sn, Pb or Ge), *Mater. Sci. Semicond. Process.*, 2021, **122**, 105484, DOI: **10.1016/j.mssp.2020.105484**.

21 Y. Selmani, H. Labrim, M. Mouatassime and L. Bahmad, Structural, optoelectronic and thermoelectric properties of Cs-based fluoroperovskites $CsMF_3$ (M= Ge, Sn or Pb), *Mater. Sci. Semicond. Process.*, 2022, **152**, 107053, DOI: **10.1016/j.mssp.2022.107053**.

22 A. Srivastava, *et al.*, Lead Metal Halide Perovskite Solar Cells: Fabrication, Advancement Strategies, Alternatives, and Future perspectives, *Mater. Today Commun.*, 2023, 105686, DOI: **10.1016/j.mtcomm.2023.105686**.

23 Z. Xu, *et al.*, Functional Layers of Inverted Flexible Perovskite Solar Cells and Effective Technologies for Device Commercialization, *Small Struct.*, 2023, **4**(5), DOI: **10.1002/sstr.202200338**.

24 Q. Xia, *et al.*, All-Solid-State Thin Film Lithium/Lithium-Ion Microbatteries for Powering the Internet of Things, *Adv. Mater.*, 2022, **35**(2), 2200538, DOI: **10.1002/adma.202200538**.

25 B. K. Ravidas, M. K. Roy and D. P. Samajdar, Investigation of photovoltaic performance of lead-free $CsSnI_3$-based perovskite solar cell with different hole transport layers: First Principles Calculations and SCAPS-1D Analysis, *Sol. Energy*, 2023, **249**, 163–173, DOI: **10.1016/j.solener.2022.11.025**.

26 J. Zhang, X. Gao, Y. Deng, Y. Zha and C. Yuan, Comparison of life cycle environmental impacts of different perovskite solar cell systems, *Sol. Energy Mater. Sol. Cells*, 2017, **166**, 9–17, DOI: **10.1016/j.solmat.2017.03.008**.

27 G. Nasti and A. Abate, Tin Halide Perovskite $(ASnX_3)$ Solar Cells: A Comprehensive Guide toward the Highest Power Conversion Efficiency, *Adv. Energy Mater.*, 2019, 1902467, DOI: **10.1002/aenm.201902467**.

28 Po K. Kung, *et al.*, Lead-Free Double Perovskites for Perovskite Solar Cells, *Sol. RRL*, 2019, **4**(2), DOI: **10.1002/solr.201900306**.

29 A. E. Maughan, A. M. Ganose, D. O. Scanlon and J. R. Neilson, Perspectives and Design Principles of Vacancy-Ordered Double Perovskite Halide Semiconductors, *Chem. Mater.*, 2019, **31**(4), 1184–1195, DOI: **10.1021/acs.chemmater.8b05036**.

30 V. Pecunia, L. G. Occhipinti, A. Chakraborty, Y. Pan and Y. Peng, Lead-free halide perovskite photovoltaics: Challenges, open questions, and opportunities, *APL Mater.*, 2020, **8**(10), 100901, DOI: **10.1063/5.0022271**.

31 Q. Sun, W.-J. Yin and S.-H. Wei, Searching for stable perovskite solar cell materials using materials genome techniques and high-throughput calculations, *J. Mater. Chem. C*, 2020, **8**(35), 12012–12035, DOI: **10.1039/d0tc02231d**.

32 Y. Wu, L. Qiu, J. Liu, M. Guan, Z. Dai and G. Li, Narrow Bandgap Metal Halide Perovskites: Synthesis, Characterization, and Optoelectronic Applications, *Adv. Opt. Mater.*, 2022, **10**(11), 2102661, DOI: **10.1002/adom.202102661**.

33 X. Wang, T. Zhang, Y. Lou and Y. Zhao, All-inorganic lead-free perovskites for optoelectronic applications, *Mater. Chem. Front.*, 2019, **3**(3), 365–375, DOI: **10.1039/c8qm00611c**.

34 K. Kuhar, *et al.*, Sulfide perovskites for solar energy conversion applications: computational screening and synthesis of the selected compound $LaYS_3$, *Energy Environ. Sci.*, 2017, **10**(12), 2579–2593, DOI: **10.1039/c7ee02702h**.

35 D. Tiwari, O. S. Hutter and G. Longo, Chalcogenide perovskites for photovoltaics: current status and prospects, *J. Phys.: Energy*, 2021, **3**(3), 034010, DOI: **10.1088/2515-7655/abf41c**.

36 Y. Nishigaki, *et al.*, Extraordinary Strong Band-Edge Absorption in Distorted Chalcogenide Perovskites, *Sol. RRL*, 2020, **4**(5), 1900555, DOI: **10.1002/solr.201900555**.

37 M. D. Kassa, N. G. Debelo and M. M. Woldemariam, The study of structural, electronic, and optical properties of Ti- substituted CaZr1-xTix S₃ (x=0.00, 0.25, 0.50, 0.75, and 1.00) for optoelectronic applications: Using GGA and GGA+U, *Solid State Commun.*, 2023, **371**, 115255, DOI: **10.1016/j.ssc.2023.115255**.

38 M. A. Ghebouli, B. Ghebouli, R. Larbi, T. Chihi and M. Fatmi, Effect of buffer nature, absorber layer thickness and temperature on the performance of CISSe based solar cells, using SCAPS-1D simulation program, *Optik*, 2021, **241**, 166203, DOI: **10.1016/j.ijleo.2020.166203**.

39 A. Talbi, Y. Khaaissa, K. Nouneh, El M. Feddi and M. E. Haouari, Effects of temperature, thickness, electron density and defect density on ZnS based solar cells: SCAPS-1D simulation, *Mater. Today: Proc.*, 2022, **66**, 116–121, DOI: **10.1016/j.matpr.2022.03.694**.

40 K. Shivesh, I. Alam, A. K. Kushwaha, M. Kumar and S. V. Singh, Investigating the theoretical performance of Cs₂TiBr₆ -based perovskite solar cell with La-doped BaSnO₃ and CuSbS₂ as the charge transport layers, *Int. J. Energy Res.*, 2021, **46**(5), 6045–6064, DOI: **10.1002/er.7546**.

41 F. Kherrat, *et al.*, Performance enhancement of eco-friendly Cs₃Sb₂I₉-based perovskite solar cell employing Nb₂O₅ and CuI as efficient charge transport layers, *Micro Nanostruct.*, 2023, **183**, 207676, DOI: **10.1016/j.micrna.2023.207676**.

42 C. Devi and R. Mehra, Device simulation of lead-free MASnI₃ solar cell with CuSbS₂ (copper antimony sulfide), *J. Mater. Sci.*, 2019, **54**(7), 5615–5624, DOI: **10.1007/s10853-018-03265-y**.

43 M. Liu, M. B. Johnston and H. J. Snaith, Efficient planar heterojunction perovskite solar cells by vapour deposition, *Nature*, 2013, **501**(7467), 395–398, DOI: **10.1038/nature12509**.

44 M. Khalid Hossain, *et al.*, Efficiency enhancement of natural dye sensitized solar cell by optimizing electrode fabrication parameters, *Mater. Sci.-Pol.*, 2017, **35**(4), 816–823, DOI: **10.1515/msp-2017-0086**.

45 P. Basera and S. Bhattacharya, Chalcogenide Perovskites (ABS₃; A = Ba, Ca, Sr; B = Hf, Sn): An Emerging Class of Semiconductors for Optoelectronics, *J. Phys. Chem. Lett.*, 2022, **13**(28), 6439–6446, DOI: **10.1021/acs.jpclett.2c01337**.

46 A. D. Adewoyin, M. A. Olopade and M. Chendo, Prediction and optimization of the performance characteristics of CZTS thin film solar cell using band gap grading, *Opt. Quantum Electron.*, 2017, **49**(10), DOI: **10.1007/s11082-017-1176-3**.

47 G. Kresse and J. Furthmüller, Efficient iterative schemes forab initiototal-energy calculations using a plane-wave basis set, *Phys. Rev. B:Condens. Matter Mater. Phys.*, 1996, **54**(16), 11169–11186, DOI: **10.1103/physrevb.54.11169**.

48 P. E. Blöchl, Projector augmented-wave method, *Phys. Rev. B:Condens. Matter Mater. Phys.*, 1994, **50**(24), 17953–17979, DOI: **10.1103/physrevb.50.17953**.

49 S. Baroni, S. de Gironcoli, A. D. Corso and P. Giannozzi, Phonons and related crystal properties from density-functional perturbation theory, *Rev. Mod. Phys.*, 2001, **73**(2), 515–562, DOI: **10.1103/RevModPhys.73.515**.

50 E. Danladi, P. M. Gyuk, N. N. Tasie, A. C. Egbugha, D. Behera, I. Hossain, I. M. Bagudo, M. L. Madugu and J. T. Ikyumbur, Impact of hole transport material on perovskite solar cells with different metal electrode: A SCAPS-1D simulation insight, *Heliyon*, 2023, **9**(6), e16838, DOI: **10.1016/j.heliyon.2023.e16838**.

51 M. K. Hossain, *et al.*, An extensive study on multiple ETL and HTL layers to design and simulation of high-performance lead-free CsSnCl₃-based perovskite solar cells, *Sci. Rep.*, 2023, **13**(1), DOI: **10.1038/s41598-023-28506-2**.

52 A. Talbi, Y. Khaaissa, K. Nouneh, El M. Feddi and M. E. Haouari, Effects of temperature, thickness, electron density and defect density on ZnS based solar cells: SCAPS-1D simulation, *Mater. Today: Proc.*, 2022, **66**, 116–121, DOI: **10.1016/j.matpr.2022.03.694**.

53 M. A. Ghebouli, B. Ghebouli, R. Larbi, T. Chihi and M. Fatmi, Effect of buffer nature, absorber layer thickness and temperature on the performance of CISSe based solar cells, using SCAPS-1D simulation program, *Optik*, 2021, **241**, 166203, DOI: **10.1016/j.ijleo.2020.166203**.

54 M. K. Hossain, *et al.*, Optimization of the architecture of lead-free CsSnCl₃-perovskite solar cells for enhancement of efficiency: A combination of SCAPS-1D and wxAMPS study, *Mater. Chem. Phys.*, 2023, **308**, 128281, DOI: **10.1016/j.matchemphys.2023.128281**.

55 S. Yamaoka and B. Okai, Preparations of BaSnS₃, SrSnS₃ and PbSnS₃ at high pressure, *Mater. Res. Bull.*, 1970, **5**(10), 789–794, DOI: **10.1016/0025-5408(70)90093-0**.

56 R. Lelieveld and D. J. W. Ijdo, Lead zirconium sulphide, *Acta Crystallogr.*, 1978, **34**(11), 3348–3349, DOI: **10.1107/S0567740878010882**.

57 C. P. Sujith, T. Mathew and V. Mathew, Density functional study of electronic and optical properties of quasi-one-dimensional metal tin sulfides MSnS₃ (M=Hf, Zr), *Solid State Sci.*, 2021, **116**, 106608, DOI: **10.1016/j.solidstatesciences.2021.106608**.

58 X. Wang, *et al.*, Double dual-nodal-line semimetals with large surface density of states: Topological quantum catalysts for the hydrogen-evolution reaction, *Phys. Rev. Appl.*, 2023, **20**(4), DOI: **10.1103/physrevapplied.20.044042**.

59 J. Wang, *et al.*, 3D Carbon Allotropes: Topological Quantum Materials with Obstructed Atomic Insulating Phases, Multiple Bulk-Boundary Correspondences, and Real Topology, *Adv. Funct. Mater.*, 2024, **34**(30), DOI: **10.1002/adfm.202316079**.

60 S. Mahmud, M. M. Hossain, M. M. Uddin and M. A. Ali, Prediction of X₂AuYZ₆ (X = Cs, Rb; Z = Cl, Br, I) double halide perovskites for photovoltaic and wasted heat management device applications, *J. Phys. Chem. Solids*, 2024, **196**, 112298, DOI: **10.1016/j.jpcs.2024.112298**.

61 M. U. Salma and Md. Atikur Rahman, Study of structural, elastic, electronic, mechanical, optical and

thermodynamic properties of $NdPb_3$ intermetallic compound: DFT based calculations, *Comput. Condens. Matter*, 2018, **15**(1), 42–47, DOI: **10.1016/j.cocom.2018.04.001**.

62 M. Markov, *et al.*, Semi-metals as potential thermoelectric materials, *Sci. Rep.*, 2018, **8**(1), 9876, DOI: **10.1038/s41598-018-28043-3**.

63 D. J. Singh, D. A. Papaconstantopoulos, J. P. Julien and F. Cyrot-Lackmann, Electronic structure of $Ba(Sn,Sb)O_3$: Absence of superconductivity, *Phys. Rev. B:Condens. Matter Mater. Phys.*, 1991, **44**(17), 9519–9523, DOI: **10.1103/physrevb.44.9519**.

64 S. Rühle, Tabulated values of the Shockley–Queisser limit for single junction solar cells, *Sol. Energy*, 2016, **130**, 139–147, DOI: **10.1016/j.solener.2016.02.015**.

65 W. Gao, *et al.*, High-Quality $Cs_2AgBiBr_6$ Double Perovskite Film for Lead-Free Inverted Planar Heterojunction Solar Cells with 2.2% Efficiency, *ChemPhysChem*, 2018, **19**(14), 1696–1700, DOI: **10.1002/cphc.201800346**.

66 M. Saeed Shadabroo, H. Abdizadeh and M. R. Golobostanfard, Elpasolite structures based on A_2AgBiX_6 (A: MA, Cs, X: I, Br): Application in double perovskite solar cells, *Mater. Sci. Semicond. Process.*, 2021, **125**, 105639, DOI: **10.1016/j.mssp.2020.105639**.

67 M. Wang, *et al.*, High-Quality Sequential-Vapor-Deposited $Cs_2AgBiBr_6$ Thin Films for Lead-Free Perovskite Solar Cells, *Sol. RRL*, 2018, **2**(12), 1800217, DOI: **10.1002/solr.201800217**.

68 S. Lee, *et al.*, Giant magneto-elastic coupling in multiferroic hexagonal manganites, *Nature*, 2008, **451**(7180), 805–808, DOI: **10.1038/nature06507**.

69 S. Li, R. Ahuja, M. W. Barsoum, P. Jena and B. Johansson, Optical properties of Ti_3SiC_2 and Ti_4AlN_3, *Appl. Phys. Lett.*, 2008, **92**(22), 221907, DOI: **10.1063/1.2938862**.

70 Y. Pan and F. Yang, The influence of pressure on the structural stability, mechanical, electronic and optical properties of TiH_4 and VH_4 tetrahydrides: A first-principles study, *Ceram. Int.*, 2024, **50**(9), DOI: **10.1016/j.ceramint.2024.01.401**.

71 J. Sólyom, *Optical Properties of Solids*, Springer eBooks, 2008, pp. 411–447, DOI: **10.1007/978-3-540-85316-9_10**.

72 A. Kojima, K. Teshima, Y. Shirai and T. Miyasaka, Organometal Halide Perovskites as Visible-Light Sensitizers for Photovoltaic Cells, *J. Am. Chem. Soc.*, 2009, **131**(17), 6050–6051, DOI: **10.1021/ja809598r**.

73 M. Caid, D. Rached, Y. Rached and H. Rached, Comprehensive exploration of halide double perovskites $Cs_2B'GeCl_6$ (B′: Zn, Cd) for affordable energy technologies: a high-throughput investigation, *Opt. Quantum Electron.*, 2024, **56**(6), DOI: **10.1007/s11082-024-06721-z**.

74 S. Gohri, *et al.*, Achieving 24.6% efficiency in 2D perovskite solar cells: Bandgap tuning and MXene contact optimization in $(BDA)(MA)_{n-1}PbnI_{3n+1}$ structures, *Chem. Phys. Lett.*, 2024, **845**, 141291, DOI: **10.1016/j.cplett.2024.141291**.

75 I. Alam, R. Mollick and M. A. Ashraf, Numerical simulation of $Cs_2AgBiBr_6$-based perovskite solar cell with ZnO nanorod

76 and P_3HT as the charge transport layers, *Phys. B*, 2021, **618**, 413187, DOI: **10.1016/j.physb.2021.413187**.

76 S. M. Sze and K. K. Ng, *Physics of Semiconductor Devices*, Hoboken, Nj, Wiley-Interscience, 2006.

77 U. Mandadapu, Simulation and Analysis of Lead based Perovskite Solar Cell using SCAPS-1D, *Indian J. Sci. Technol.*, 2017, **10**(1), 1–8, DOI: **10.17485/ijst/2017/v11i10/110721**.

78 M. S. Jamal, *et al.*, Effect of defect density and energy level mismatch on the performance of perovskite solar cells by numerical simulation, *Optik*, 2019, **182**, 1204–1210, DOI: **10.1016/j.ijleo.2018.12.163**.

79 S. Ijaz, *et al.*, A numerical approach to optimize the performance of HTL-free carbon electrode-based perovskite solar cells using organic ETLs, *Heliyon*, 2024, **10**(7), e29091, DOI: **10.1016/j.heliyon.2024.e29091**.

80 Md. Samiul Islam, *et al.*, Defect Study and Modelling of SnX3-Based Perovskite Solar Cells with SCAPS-1D, *Nanomaterials*, 2021, **11**(5), 1218, DOI: **10.3390/nano11051218**.

81 N. Singh, A. Agarwal and M. Agarwal, Numerical simulation of highly efficient lead-free all-perovskite tandem solar cell, *Sol. Energy*, 2020, **208**, 399–410, DOI: **10.1016/j.solener.2020.08.003**.

82 C. Devi and R. Mehra, Device simulation of lead-free $MASnI_3$ solar cell with $CuSbS_2$ (copper antimony sulfide), *J. Mater. Sci.*, 2019, **54**(7), 5615–5624, DOI: **10.1007/s10853-018-03265-y**.

83 V. Adinolfi, *et al.*, The In-Gap Electronic State Spectrum of Methylammonium Lead Iodide Single-Crystal Perovskites, *Adv. Mater.*, 2016, **28**(17), 3406–3410, DOI: **10.1002/adma.201505162**.

84 G. G. Malliaras, J. R. Salem, P. J. Brock and C. Scott, Electrical characteristics and efficiency of single-layer organic light-emitting diodes, *Phys. Rev. B:Condens. Matter Mater. Phys.*, 1998, **58**(20), R13411–R13414, DOI: **10.1103/physrevb.58.r13411**.

85 K. Decock, S. Khelifi and M. Burgelman, Modelling multivalent defects in thin film solar cells, *Thin Solid Films*, 2011, **519**(21), 7481–7484, DOI: **10.1016/j.tsf.2010.12.039**.

86 Md. Samiul Islam, *et al.*, Defect Study and Modelling of SnX3-Based Perovskite Solar Cells with SCAPS-1D, *Nanomaterials*, 2021, **11**(5), 1218, DOI: **10.3390/nano11051218**.

87 P. Y. Yu and M. Cardona, *Fundamentals of Semiconductors: Physics and Materials Properties*, Berlin, Heidelberg, Springer Berlin Heidelberg, 2010.

88 B. Ḿonemar, Fundamental energy gap of GaN from photoluminescence excitation spectra, *Phys. Rev. B:Condens. Matter Mater. Phys.*, 1974, **10**(2), 676–681, DOI: **10.1103/physrevb.10.676**.

89 Y. P. Varshni, Temperature dependence of the energy gap in semiconductors, *Physica*, 1967, **34**(1), 149–154, DOI: **10.1016/0031-8914(67)90062-6**.

90 C. Sun, Y. Zou, C. Qin, B. Zhang and X. Wu, Temperature effect of photovoltaic cells: a review, *Adv. Compos. Hybrid*

Mater., 2022, **5**(4), 2675–2699, DOI: **10.1007/s42114-022-00533-z**.

91 P. Geng, W. Li, X. Zhang, Y. Deng and H. Kou, A novel theoretical model for the temperature dependence of band gap energy in semiconductors, *J. Phys. D:Appl. Phys.*, 2017, **50**(40), 40LT02, DOI: **10.1088/1361-6463/aa85ad**.

92 A. S. Yusuf, A. M. Ramalan, A. A. Abubakar and I. K. Mohammed, Effect of Electron Transport Layers, Interface Defect Density and Working Temperature on Perovskite Solar Cells Using SCAPS 1-D Software, *East Eur. J. Phys.*, 2024, (1), 332–341, DOI: **10.26565/2312-4334-2024-1-31**.

93 Md. Ferdous Rahman, *et al.*, Design and numerical investigation of cadmium telluride (CdTe) and iron silicide (FeSi$_2$) based double absorber solar cells to enhance power conversion efficiency, *AIP Adv.*, 2022, **12**(10), DOI: **10.1063/5.0108459**.

94 B. Barman and S. Ingole, Analysis of Si Back-Contact for Chalcogenide Perovskite Solar Cells Based on BaZrS$_3$ Using SCAPS-1D, *Adv. Theory Simul.*, 2023, **6**(7), DOI: **10.1002/adts.202200820**.

95 M. K. Hossain, *et al.*, An extensive study on multiple ETL and HTL layers to design and simulation of high-performance lead-free CsSnCl$_3$-based perovskite solar cells, *Sci. Rep.*, 2023, **13**(1), DOI: **10.1038/s41598-023-28506-2**.

96 F. B. Sumona, *et al.*, Optimization of Perovskite-KSnI$_3$ Solar Cell by Using Different Hole and Electron Transport Layers: A Numerical SCAPS-1D Simulation, *Energy Fuels*, 2023, **37**(23), 19207–19219, DOI: **10.1021/acs.energyfuels.3c02397**.

97 M. Ahamad and A. K. M. A. Hossain, Design and optimization of non-toxic and highly efficient tin-based organic perovskite solar cells by device simulation, *Heliyon*, 2023, **9**(9), e19389, DOI: **10.1016/j.heliyon.2023.e19389**.

98 A. Yousfi and W. Feneniche, Effect of Graded Double Perovskite for Boosting up the Photovoltaic Output Parameters of Solar Cell: A Numerical Modelling Using SCAPS-1D, *J. Nano- Electron. Phys.*, 2023, **15**(6), **https://essuir.sumdu.edu.ua/handle/123456789/94032**.

99 M. Khalid Hossain, *et al.*, Achieving above 24% efficiency with non-toxic CsSnI$_3$ perovskite solar cells by harnessing the potential of the absorber and charge transport layers, *RSC Adv.*, 2023, **13**(34), 23514–23537, DOI: **10.1039/d3ra02910g**.

100 N. Thakur, P. Kumar and P. Sharma, Simulation study of chalcogenide perovskite (BaZrSe3) solar cell by SCAPS-1D, *Mater. Today: Proc.*, 2023, (Part 1), 584–589, DOI: **10.1016/j.matpr.2023.01.012**.

101 S. Kumar, L. Allam, S. Bharadwaj and B. Barman, Enhancing SrZrS3 Perovskite Solar Cells: A Comprehensive SCAPS-1D Analysis of Inorganic Transport Layers, *J. Phys. Chem. Solids*, 2024, **196**, 112378, DOI: **10.1016/j.jpcs.2024.112378**.

102 S. Yamaoka and B. Okai, Preparations of BaSnS3, SrSnS3 and PbSnS3 at high pressure, *Mater. Res. Bull.*, 1970, **5**(10), 789–794, DOI: **10.1016/0025-5408(70)90093-0**.

103 R. Woods-Robinson, K. A. Persson and A. Zakutayev, Stability and synthesis across barium tin sulfide material space, *J. Mater. Chem. A*, 2023, **11**(45), 24948–24958, DOI: **10.1039/d3ta04431a**.

104 S. Agarwal, K. C. Vincent and R. Agrawal, From synthesis to application: a review of BaZrS$_3$ chalcogenide perovskites, *Nanoscale*, 2025, **17**(8), 4250–4300, DOI: **10.1039/d4nr03880k**.

105 C. Comparotto, P. Ström, O. Donzel-Gargand, T. Kubart and J. J. S. Scragg, Synthesis of BaZrS$_3$ Perovskite Thin Films at a Moderate Temperature on Conductive Substrates, *ACS Appl. Energy Mater.*, 2022, **5**(5), 6335–6343, DOI: **10.1021/acsaem.2c00704**.

106 A. A. Pradhan, *et al.*, Synthesis of BaZrS$_3$ and BaHfS$_3$ Chalcogenide Perovskite Films Using Single-Phase Molecular Precursors at Moderate Temperatures, *Angew. Chem., Int. Ed.*, 2023, **62**(15), DOI: **10.1002/anie.202301049**.